# Accepted Manuscript


Enriched mixed finite element models for dynamic analysis of continuous and fractured porous media

M. Komijani, R. Gracie

PII: S0045-7825(18)30397-9
DOI: https://doi.org/10.1016/j.cma.2018.08.011
Reference: CMA 12025

To appear in: *Comput. Methods Appl. Mech. Engrg.*

Received date : 9 November 2017
Revised date : 18 May 2018
Accepted date : 5 August 2018

Please cite this article as: M. Komijani, R. Gracie, Enriched mixed finite element models for dynamic analysis of continuous and fractured porous media, *Comput. Methods Appl. Mech. Engrg.* (2018), https://doi.org/10.1016/j.cma.2018.08.011

**Highlights (for review)**

- Presentation of improved methods for the simulation of the dynamics of continuous and discontinuous porous media.

- Presentation of the first application of the Phantom Node Method (PNM) to model fractures in porous media.

- Illustration that GFEM enrichment with suitable trigonometric functions can significantly reduce the spurious oscillations which appear in FEM simulations of wave phenomena in porous media.

- Presentation of a mixed Generalized Finite Element Method coupled with a PNM (PNM-GFEMM) to more accurately model wave propagation in fractured porous media.

- Presentation of an Augmented Lagrangian Method to implement contact and stick-slip friction between fracture surfaces, in the context of the PNM and the PNM-GFEM-M.

# Enriched Mixed Finite Element Models for Dynamic Analysis of Continuous and Fractured Porous Media

M. Komijani, R. Gracie*

*Department of Civil and Environmental Engineering, University of Waterloo, Waterloo, Ontario, Canada*

**Abstract**

Enriched Finite Element Models are presented to more accurately investigate the transient and wave propagation responses of continuous and fractured porous media based on mixture theory. Firstly, the Generalized Finite Element Method (GFEM) trigonometric enrichments are introduced to suppress the spurious oscillations that may appear in dynamic analysis with the regular Finite Element Method (FEM) due to numerical dispersion/Gibb's phenomenon. Secondly, the Phantom Node Method (PNM) is employed to model multiple arbitrary fractures independently of the mesh topology. Thirdly, frictional contact behaviour is simulated using an Augmented Lagrange Multiplier technique. Mixed Lagrangian interpolants, bi-quadratic for displacements and bi-linear for pore pressure, are used for the underlying FEM basis. Transient (non-wave propagation) response of fractured porous media is effectively modeled using the PNM. Wave propagation in continuous porous media is effectively modeled using the mixed GFEM. Wave propagation in fractured porous media is accurately simulated using a mixed GFEM-enriched Phantom Node Method (PNM-GFEM-M). The developed mixed GFEM portion of the model is verified through a transient consolidation problem. Subsequently, the ability of the enriched FEM models to capture the dynamic response of fractured fully-saturated porous media under mechanical and hydraulic stimulations is illustrated. The superior ability of the PNM-GFEM-M to inhibiting spurious oscillations is shown in comparison against the regular finite element solutions of some impact problems. **It is demonstrated that by embedding appropriate enrichment basis functions in both displacement and pore pressure fields the results obtained are more accurate than those obtained using standard finite element approximations or approximations in which only the displacement is enriched.**

*Keywords:*
Generalized finite element method, Phantom node method, Porous media, Dynamic response, Wave propagation.

## 1. Introduction

Analysis of porous media is of importance in a wide range of applications from reservoir engineering to biological materials. Accurate simulation of coupled behaviour of fluid and solid in geomechanics is essential in improving the reservoir performance and ensuring wellbore stability[1]. In a similar fashion, biomechanical analysis of tissues such as the brain, bones, and cells involves coupled behaviour of solid skeleton and a pore fluid [2, 3, 4, 5]. Investigations of coupled hydro-mechanical problems has a relatively long history going back to the pioneering works of Terzaghi [6] and Biot [7].

Dynamic analysis is important in application such as liquefaction, induced seismicity, and earthquake analysis, in which inertia effects are of significance. In coupled analysis of porous media, different approaches have been developed to model the hydro-mechanical response. Fully-dynamic three-field models ($u-w-p$) have been used to solve the problem based on the solution for solid skeleton displacement, $u$, the displacement of the fluid relative to the solid matrix, $w$, and the fluid pore pressure, $p$ [8, 9]. In some other works, based on the assumption that the relative acceleration of fluid with respect to the total mixture is negligible,

*Corresponding author. E-mail address: rgracie@uwaterloo.ca.

a simpler two-field formulations $(u-p)$ had been developed [10]. Alternative formulation based on the same assumption has lead to $(u-w)$ models, in which pore pressure is eliminated instead of the relative displacement of fluid with respect to the solid skeleton [12, 13] . Two-field $u-p$ models of porous media have been noted to be more appropriate for modelling saturated porous material up to earthquake frequencies [14].

Previous research efforts in dynamic/wave propagation analysis of porous media have emphasized the hydro-mechanical response of continuous domains. However, in many applications, such as the analysis of naturally fractured rock masses, we encounter discontinuous domains which contain pre-existing or induced cracks and/or faults. The analysis of microseismic emission due to the reactivation of natural fractures in geological formations under high in-situ stresses is of practical importance in the evolution of hydraulic fracturing operations, which has not been dealt with sufficiently in the literature so far.

The dominant approach in seismic analysis has been to solve wave propagation in frequency domain [15] with the assumption that the simulation domain is continuous and does not contain any fractures; in spite the fact that the coupled problem of micro-seismic emission due to fault reactivation has to be partially modeled (in localization/crack propagation phase) in the time domain. Therefore, developing new and efficient time domain-based computational methods and tools to simulate the dynamic hydro-mechanical response of porous systems that include discontinuities seems to be necessary and practical.

In the area of fractured porous media analysis, Remij et al. [16] present an enhanced local pressure model for simulation of fluid-driven fractures in porous media using partition-of-unity finite element to impose strong discontinuity of displacement and pressure fields across the fracture. In this work, fracture propagation due to internal flow is modeled by a cohesive traction-separation law. Nikolic et al. [17] proposed a discrete beam lattice model for simulation of localization in a fluid-saturated poro-plastic media. Localized failure of media is embedded through discontinuities located in cohesive links enabled by the proposed discrete model which can capture the fracture process zone initiation and the localization mechanisms. Armero and Callari [19] performed an analysis of strong discontinuities in displacement in a poroplastic solid. They considered continuous pressure field across the material discontinuity with discontinuous pressure gradient leading to discontinuous fluid flux across the crack. They used an enhanced strain finite element formulation to represent the normal and shear displacement jumps along the discontinuity. Rethore et al. [18] developed a numerical model for dynamic propagation of shear bands in saturated porous media. They used the partition of unity property of finite element to introduce discontinuity in the domain in the context of XFEM. Using cohesive shear tractions they simulated nucleation and propagation of shear bands based on Tresca-like and a Coulomb criterion.

Another approach for simulation of fracture in porous media has been the phase field modeling. Christian Miehe and Steffen Mauthe [20] proposed a macroscopic framework for a continuum phase field modeling of fracture in porous media. The main idea in this approach is to regularize the discrete crack based on a constitutive balance equation. The approach overcomes difficulties associated with the computational realization of sharp discontinuities which is involved in discontinuity modeling and specifying the trajectory of fracture once it propagates. The multi-physics coupling of porous media is accommodated through a modular concept for linking of the diffusive crack modeling with the hydro-poro-elastic response of the porous bulk material. Lee et al. [21] employed phase field approach for proppant-filled fractures in porous media to solve for displacements, phase field, pressure, and proppant concentration though a continuum model. The coupling to the pressure equation is imposed via a fixed-stress iteration. A diffraction equation is used to obtain the pressure and the phase-field variable serves as an indicator function that distinguishes between the fracture and the reservoir. In this context, some damage localization models have also been proposed for porous media. Mobasher et al. [22] proposed a damage-poroelastic model for analyzing the localization of porous media in geomechanics applications. The mesh-dependency problem of local damage models has been rectified by introducing a non-local model. However, these earlier works that are proposed to model fracture in porous media did not address the topic of accurate simulation of wave propagation in multi-physics media.

To model arbitrary fractures independently of mesh topology and to rectify the requirement for continuous re-meshing in the process of crack propagation Moes et al. [23] developed the concept of the eXtended

Finite Element Model (XFEM). XFEM is based on the general idea of the Partition of Unity Finite Element Method [24]. As a continuation, Song et al. [28] introduced and developed the idea of Phantom Node Method (PNM) to model discontinuities. The model is in essence the same as the earlier method proposed by Hansbo and Hansbo [29]. In the PNM, discontinuity in displacement is achieved by reformulating elements, which contain a fracture as two superimposed intact elements with additional computational nodes, called Phantom Nodes. Each of the superimposed elements is used to represent a different side of the original cracked element, resulting in a discontinuous interpolation for displacement. The most important feature and advantage of the PNM is that its implementation requires fewer modifications to an existing FEM code compared to XFEM. To date the PNM has only been applied to purely mechanical models. Here we extend its application to fractured porous media.

Owing to the direct satisfaction of the natural boundary conditions through integral form of the weak formulation (divergence theorem), finite element is known to be a very effective tool for solving boundary-value problems. However, the piecewise continuous polynomials used to interpolate the unknown functions have been found to be inadequate in some problems, including transient wave propagation [35]. In the case of transient wave propagation, FEM solution may show spurious oscillations. These non-physical oscillations degrade the results, including the wave propagation velocity, which is important in application such as microseismic wave simulation, where the waves travel long distances. Here, this problem is treated through introduction of harmonic enrichments.

An enriched finite element method was proposed in [34], where enriched harmonic and conventional low-order polynomials interpolations are used to model multiscale wave propagation in one-dimensional problems. The general idea of embedding appropriate basis functions, with characteristics that appear in the analytical solution of the problem, as enrichments using the partition of unity property of the FE interpolants was developed in the pioneering work of Melenk and Babuka [24]. **For more detailed information about enriched finite element methods one can also refer to [25, 26, 27]**. Based on the general idea of the Partition of Unity Method (PUM), Ham and Bahte [35] extended the approach of [34] to solve the problem of time-harmonic and transient wave propagation in multiple dimensions; it was demonstrated that the spurious oscillations that appear with the conventional FEM can effectively subside by the proposed enriched FEM in the simulation of wave propagation in continuous domains.

Very recently, a GFEM-enriched PNM model was proposed by Komijani and Gracie [36] to extend the enriched FE model developed in [35] to the case of fractured media. Their enriched FE model, the PNM-GFEM, combines the advantages of the trigonometric enrichments introduced in [35] and the Phantom Node Method. Using the PNM-GFEM, problem of transient wave propagation in fractured media is simulated in various cases of high-frequency/impact mechanical loading conditions. Through several numerical illustrations it was demonstrated that the high-frequency non-physical spurious oscillations can be dramatically suppressed in both primary emitted waves and reflected waves from the fracture surfaces.

To date these enriched finite element models have not been applied to any coupled multi-physics problem with or without discontinuities, such as fractured porous media. The purpose of the present article is to extend the use of the PNM-GFEM enriched FE model introduced in [36] to the case of fractured saturated porous media. GFEM trigonometric functions are used to enrich the displacement field of solid skeleton and pore pressure field to model transient wave propagation response of porous media more accurately. The PNM is employed in a combined fashion to simulate discontinuities in the displacement fields as well as pore pressure field in the case of impervious crack faces. The dynamic behaviour of fractured porous media is investigated through several numerical examples for different mechanical and hydraulic loading types.

## 2. Mathematical Formulation

A porous media is composed of a fluid filled solid matrix. The fluid phase can flow through the connected voids of the solid matrix. The behaviour of a porous media is governed by the interaction of fluid and solid phases. In this work, the governing equations are obtained from Biot's mixture theory based on the concept

of volume fractions for each phase in a representative elementary volume.

### 2.1. Governing Equations

Consider a two-dimensional poroelastic medium, $\Omega$, defined in Cartesian coordinate $O_{xy}$. Let $u_x(x, y, t)$ and $u_y(x, y, t)$ be the displacement components of the total mixture in $x$ and $y$ directions, respectively, as a function of time, $t$. Assuming infinitesimal deformation, the linear strain-displacement relations are

$$\varepsilon_{xx} = u_{x,x} \qquad \varepsilon_{yy} = u_{y,y} \qquad \gamma_{xy} = u_{x,y} + u_{y,x} \tag{1}$$

The constitutive equations for the solid matrix can be written in Voigt notation as:

$$\begin{bmatrix} \sigma'_{xx} \\ \sigma'_{yy} \\ \sigma'_{xy} \end{bmatrix} = \begin{bmatrix} C_{11} & C_{12} & 0 \\ C_{21} & C_{22} & 0 \\ 0 & 0 & C_{33} \end{bmatrix} \begin{bmatrix} \varepsilon_{xx} \\ \varepsilon_{yy} \\ \gamma_{xy} \end{bmatrix} \tag{2}$$

in which $\sigma'_{xx}$, $\sigma'_{yy}$, and $\sigma'_{xy}$ are the components of the effective stress tensor acting on the solid skeleton, and $C_{11}$ through $C_{33}$ are the elastic coefficients.

The relative motion of the fluid phase with respect to the total mixture is denoted by $w_i(x, t)$; it is assumed that the relative acceleration of the fluid phase with respect to the entire mixture is negligible, i.e., $\ddot{w}_i = 0$. The momentum balance of the total mixture is:

$$\nabla \cdot \boldsymbol{\sigma} - \rho \ddot{\boldsymbol{u}} + \rho \boldsymbol{b} = 0 \tag{3}$$

in which $\ddot{\boldsymbol{u}}$ is the acceleration of the total mixture, $\boldsymbol{\sigma}$ is the total stress, $\rho$ is the average mixture density, and $b$ is the body force acting on the mixture.

The average density of the mixture is defined as a linear combination of solid and fluid phases

$$\rho = n'\rho_f + (1 - n')\rho_s \tag{4}$$

in which $\rho_f$ and $\rho_s$ are the density of fluid phase and solid grains, respectively, and $n'$ is the porosity of the media, defined as the ratio of the porous volume to the total volume of the mixture.

The total stress acting on the mixture is defined as

$$\boldsymbol{\sigma} = \boldsymbol{\sigma'} - \alpha_p p \boldsymbol{I} \tag{5}$$

where $p$ is the fluid pore pressure, $\boldsymbol{I}$ is the identity tensor, $\boldsymbol{\sigma'}$ denotes the effective stress acting on the solid skeleton, and $\alpha_p$ is Biot's coefficient.

A generalized Darcy relation can be derived from conservation of momentum of the fluid phase. Neglecting the relative acceleration of the pore fluid with respect to the total mixture, the momentum equation for the fluid phase is:

$$-\nabla p + \boldsymbol{R} - \rho_f \ddot{\boldsymbol{u}} + \rho_f \boldsymbol{b} = 0 \tag{6}$$

in which $\boldsymbol{R}$ denotes the lumped/averaged viscous drag force acting on the fluid. The drag force may be defined by the Darcy seepage law

$$\dot{\boldsymbol{w}} = -\boldsymbol{k}_f \boldsymbol{R} \tag{7}$$

in which $\boldsymbol{k}_f$ denotes the permeability tensor of the porous media.

The Eulerian continuity equation for the fluid phase is:

$$\nabla \cdot \dot{\boldsymbol{w}} + \alpha \nabla \cdot \dot{\boldsymbol{u}} + \frac{\dot{p}}{Q} = 0 \tag{8}$$

in which $1/Q = (\alpha - n')/K_s + n'/K_f$, and $K_s$ and $K_f$ are the bulk moduli of solid and fluid phases, respectively.

The relative velocity of fluid phase with respect to the mixture, $\boldsymbol{w}$, can be eliminated from (8) using (6) and the Darcy seepage law (7) leading to [14]

$$\nabla \cdot k_f[-\nabla p - \rho_f \ddot{\boldsymbol{u}} + \rho_f \boldsymbol{b}] + \alpha \nabla \cdot \dot{\boldsymbol{u}} + \frac{\dot{p}}{Q} = 0 \tag{9}$$

Equations (3) and (9) along with the strain-displacement relations (1) and effective stress-strain constitutive equations (2) are solved together with boundary and initial conditions to find the displacement and pore pressure fields.

### *2.2. Weak Formulation*

Consider a 2D domain $\Omega$ with boundary $\Gamma$. Boundary $\Gamma$ comprises of $\Gamma_u$, $\Gamma_t$, $\Gamma_p$, and $\Gamma_w$, which are the boundary surface for prescribed displacement, traction, pore pressure, and out-flow flux of pore fluid, respectively. Domain $\Omega$ contains internal discontinuities (i.e., fractures) denoted by $\Gamma_d$. Using Galerkin's method the coupled system of equations (3) and (9) are transformed into a weak formulation using appropriate test functions, $\delta\boldsymbol{u}$ and $\delta p$.

**The admissible spaces of the displacement and pore pressure fields are defined as below:**

$$U = \left\{\mathbf{u}(x,y,t) | \mathbf{u}(x,y,t) \in H^1, \mathbf{u}(x,y,t) = \bar{\mathbf{u}}(t) \text{ on } \Gamma_u, \mathbf{u} \text{ discontinuous on } \Gamma_d\right\} \tag{10}$$

$$U_0 = \left\{\delta\boldsymbol{u}(x,y,t) | \delta\boldsymbol{u}(x,y,t) \in H^1, \delta\boldsymbol{u}(x,y,t) = 0 \text{ on } \Gamma_u, \delta\boldsymbol{u} \text{ discontinuous on } \Gamma_d\right\} \tag{11}$$

$$P = \left\{p(x,y,t) | p(x,y,t) \in H^1, p(x,y,t) = \bar{p}(t) \text{ on } \Gamma_p, p \text{ discontinuous on } \Gamma_d\right\} \tag{12}$$

$$P_0 = \left\{\delta p(x,y,t) | \delta p(x,y,t) \in H^1, \delta p(x,y,t) = 0 \text{ on } \Gamma_p, \delta p \text{ discontinuous on } \Gamma_d\right\} \tag{13}$$

The resulting weak form of the initial boundary value problem is

$$\int_\Omega \boldsymbol{\sigma} : \delta\boldsymbol{\varepsilon}\ d\Omega + \int_\Omega \rho \ddot{\boldsymbol{u}} \cdot \delta\boldsymbol{u}\ d\Omega - \int_{\Gamma_t} \bar{\boldsymbol{t}} \cdot \delta\boldsymbol{u}\ d\Gamma - \int_\Omega \rho \boldsymbol{b} \cdot \delta\boldsymbol{u}\ d\Omega + \int_{\Gamma_d} \bar{\boldsymbol{t_d}} \cdot \delta[[\boldsymbol{u}]]\ d\Gamma = 0, \forall \delta\boldsymbol{u} \in U_0 \tag{14}$$

$$\int_\Omega \nabla\delta p \cdot k_f \nabla p\ d\Omega + \int_\Omega \nabla\delta p k_f \cdot \rho_f \ddot{\boldsymbol{u}}\ d\Omega + \int_\Omega \delta p\ \alpha_p\ \nabla \cdot \dot{\boldsymbol{u}}\ d\Omega + \int_\Omega \delta p\ 1/Q\ \dot{p}\ d\Omega -$$
$$\int_\Omega \nabla\delta p k_f \cdot \rho_f \boldsymbol{b}\ d\Omega + \int_{\Gamma_w} \delta p(\dot{\boldsymbol{w}} \cdot \boldsymbol{n}_\Gamma)\ d\Gamma - \int_{\Gamma_d} \delta p[[\dot{\boldsymbol{w}}]] \cdot \boldsymbol{n}_{\Gamma_d}\ d\Gamma = 0, \forall \delta p \in P_0 \tag{15}$$

in which $[[\boldsymbol{u}]]$ **denotes the jump in the displacement field across the discontinuity surfaces and** $[[\dot{\boldsymbol{w}}]]$ **represents the discontinuity of fluid flux into the crack interface in both sides of the discontinuity.** $\bar{\boldsymbol{t_d}}$ denotes the internal applied traction (e.g., contact force) on the surfaces of the internal discontinuity $\Gamma_d$. **In this work natural boundary conditions are imposed on the internal interface,** $\Gamma_d$**. For the mechanical problem, the tractions on the crack surfaces are non-zero when contact is modeled or zero (traction free) when contact is not modeled. For flow problem, the fluid flux perpendicular to the fracture surfaces is zero for impermeable fractures. In the case of permeable fractures, there is no discontinuity in the pore pressure field and therefore no natural boundary condition needs to be considered on** $\Gamma_d$**.**

## 3. Enriched Mixed Finite Element Formulation

In this section, the discretization of the weak form (14)-(15) using the PNM-GFEM interpolations [36], the implementation of frictional contact using an Augmented-Lagrangian approach, the integration of the semi-discretized equations using a Generalized Newmark implicit method are discussed.

*3.1. GFEM interpolation*

Spurious waves due to the Gibbs phenomenon can be suppressed/reduced in FEM simulations of transient wave propagation in continuous domains by GFEM enrichment with appropriate functions. Inspired by the exponential- (or trigonometric-) type nature of the analytical solutions of wave problems, Ham and Bathe [35] proposed the following interpolation for displacement

$$\begin{aligned}\boldsymbol{u}(x,y,t) = \sum_I \Big( N_I \boldsymbol{u}_{I(0,0)} + \sum_{k_x=1}^{n} [N_I \phi^{C_x}_{(k_x,0)} \boldsymbol{u}^{C_x}_{I(k_x,0)} + N_I \phi^{S_x}_{(k_x,0)} \boldsymbol{u}^{S_x}_{I(k_x,0)}] + \\ \sum_{k_y=1}^{m} [N_I \phi^{C_y}_{(0,k_y)} \boldsymbol{u}^{C_y}_{I(0,k_y)} + N_I \phi^{S_y}_{(0,k_y)} \boldsymbol{u}^{S_y}_{I(0,k_y)}] + \\ \sum_{k_x=1}^{n} \sum_{k_y=1}^{m} [N_I \phi^{C+}_{(k_x,k_y)} \boldsymbol{u}^{C+}_{I(k_x,k_y)} + N_I \phi^{S+}_{(k_x,k_y)} \boldsymbol{u}^{S+}_{I(k_x,k_y)} + \\ N_I \phi^{C-}_{(k_x,k_y)} \boldsymbol{u}^{C-}_{I(k_x,k_y)} + N_I \phi^{S-}_{(k_x,k_y)} \boldsymbol{u}^{S-}_{I(k_x,k_y)}] \Big)\end{aligned} \tag{16}$$

in which $\phi^{\gamma}_{(k_x,k_y)}$ with the corresponding superscript denotes the following trigonometric enriched basis functions:

$$\phi^{C_x}_{(k_x,0)} = cos(\frac{2\pi k_x x}{\Lambda_x}), \quad \phi^{S_x}_{(k_x,0)} = sin(\frac{2\pi k_x x}{\Lambda_x}),$$

$$\phi^{C_y}_{(0,k_y)} = cos(\frac{2\pi k_y y}{\Lambda_y}), \quad \phi^{S_y}_{(0,k_y)} = sin(\frac{2\pi k_y y}{\Lambda_y})$$

$$\phi^{C+}_{(k_x,k_y)} = cos(\frac{2\pi k_x x}{\Lambda_x} + \frac{2\pi k_y y}{\Lambda_y}), \quad \phi^{S+}_{(k_x,k_y)} = sin(\frac{2\pi k_x x}{\Lambda_x} + \frac{2\pi k_y y}{\Lambda_y})$$

$$\phi^{C-}_{(k_x,k_y)} = cos(\frac{2\pi k_x x}{\Lambda_x} - \frac{2\pi k_y y}{\Lambda_y}), \quad \phi^{S-}_{(k_x,k_y)} = sin(\frac{2\pi k_x x}{\Lambda_x} - \frac{2\pi k_y y}{\Lambda_y})$$

**In the above enriched FE formulation $N_I$ are the conventional Lagrangian shape functions, $u_{I(0,0)}$ are the conventional nodal degrees of freedom, $u^{\gamma}_{I(k_x,k_y)}$ with the associated superscript $(C_x, C_y, S_x, S_y, ...)$ are the enriched nodal degree of freedom corresponding to the local node number $I$, $k_x$ and $k_y$ are the wave numbers, $n$ and $m$ are the cutoff numbers for enrichment functions in $x$ and $y$ directions, respectively, and $\Lambda_x$ and $\Lambda_y$ are wavelengths, which are assumed to be equal to the element sizes in $x$ and $y$ directions, respectively. It is noted that the cutoff numbers $n$ and $m$ are user-defined parameters and would vary between different problems. In the case of highly-transient waves or time-harmonic waves with short wave lengths, higher cutoff numbers may be required to obtained more accurate results. The excitation of different wave lengths can be modeled using different cutoff numbers, which facilitates the possibility of modelling waves with wavelengths smaller than the element size. It is important to note that considering higher cutoff numbers than 2 may lead to severe ill-conditioning problems. However, based on our experience so far, cutoff numbers of 1 or 2 is sufficient in many cases.**

**To model the dynamic/wave propagation response of fracture media, the Phantom Node Method [36] is combined with the above GFEM approximation (16). The PNM is employed to facilitate the modelling of the discontinuities and GFEM enrichments are used to more accurately model wave propagation, compared to what can be achieve with regular FEM approximations.** As illustrated in Figure 1, a cracked element containing a discontinuity is represented by two superimposed intact elements (i.e., overlapping paired elements) with real and additional phantom nodes [28]. The location of the discontinuity inside an element is defined by a level set function such that $f(x, y) = 0$ specifies the discontinuous surface. **In this work the level set is the signed distance**

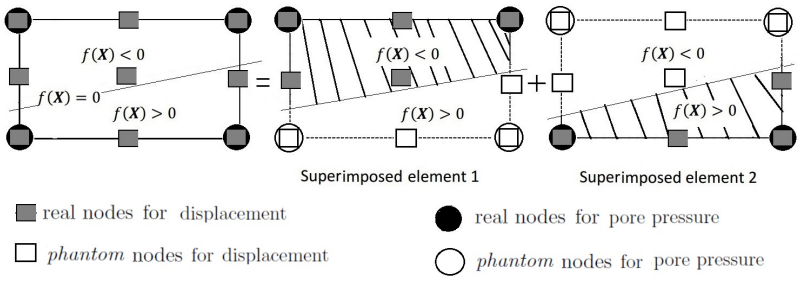


Figure 1: Decomposition of a mixed cracked element into two superimposed elements, in which the underlying Lagrangian interpolants for the displacements and pore pressure are bi-quadratic (Q9) and bi-linear (Q4) shape functions, respectively. Real and phantom nodes with displacement degrees of freedom are shown using solid and hollow rectangles, respectively. Real and phantom nodes with pore pressure degrees of freedom are shown using solid and hollow circles, respectively.

**function to the crack [28].** Displacements in fractured elements in the PNM-GFEM are approximated by

$$\begin{aligned}\boldsymbol{u}(x,y,t) = H(-f(x,y)) \sum_{I\in S_1} \Big(\psi_{I(0,0)}\boldsymbol{u}_{I(0,0)} + \sum_{k_x=1}^{n}[\psi^{C_x}_{I(k_x,0)}\boldsymbol{u}^{C_x}_{I(k_x,0)} + \psi^{S_x}_{I(k_x,0)}\boldsymbol{u}^{S_x}_{I(k_x,0)}]+ \\ \sum_{k_y=1}^{m}[\psi^{C_y}_{I(0,k_y)}\boldsymbol{u}^{C_y}_{I(0,k_y)} + \psi^{S_y}_{I(0,k_y)}\boldsymbol{u}^{S_y}_{I(0,k_y)}]+ \\ \sum_{k_x=1}^{n}\sum_{k_y=1}^{m}[\psi^{C+}_{I(k_x,k_y)}\boldsymbol{u}^{C+}_{I(k_x,k_y)} + \psi^{S+}_{I(k_x,k_y)}\boldsymbol{u}^{S+}_{I(k_x,k_y)} + \psi^{C-}_{I(k_x,k_y)}\boldsymbol{u}^{C-}_{I(k_x,k_y)} + \psi^{S-}_{I(k_x,k_y)}\boldsymbol{u}^{S-}_{I(k_x,k_y)}]\Big)+ \\ H(f(x,y)) \sum_{I\in S_2} \Big(\psi_{I(0,0)}\boldsymbol{u}_{I(0,0)} + \sum_{k_x=1}^{n}[\psi^{C_x}_{I(k_x,0)}\boldsymbol{u}^{C_x}_{I(k_x,0)} + \psi^{S_x}_{I(k_x,0)}\boldsymbol{u}^{S_x}_{I(k_x,0)}]+ \\ \sum_{k_y=1}^{m}[\psi^{C_y}_{I(0,k_y)}\boldsymbol{u}^{C_y}_{I(0,k_y)} + \psi^{S_y}_{I(0,k_y)}\boldsymbol{u}^{S_y}_{I(0,k_y)}]+ \\ \sum_{k_x=1}^{n}\sum_{k_y=1}^{m}[\psi^{C+}_{I(k_x,k_y)}\boldsymbol{u}^{C+}_{I(k_x,k_y)} + \psi^{S+}_{I(k_x,k_y)}\boldsymbol{u}^{S+}_{I(k_x,k_y)} + \psi^{C-}_{I(k_x,k_y)}\boldsymbol{u}^{C-}_{I(k_x,k_y)} + \psi^{S-}_{I(k_x,k_y)}\boldsymbol{u}^{S-}_{I(k_x,k_y)}]\Big)\end{aligned} \tag{17}$$

in which $\psi_{I(0,0)} = N_I$ and $\psi^{\gamma}_{I(k_x,k_y)} = N_I\phi^{\gamma}_{(k_x,k_y)}$, and $H(\cdot)$ is the step function. $S_1$ and $S_2$ are the set of nodes corresponding to each of the two superimposed elements; each of the two superimposed elements contain original real nodes and additional phantom nodes. In the framework of GFEM, both the real and phantom nodes have conventional and enriched degrees of freedom. **For cracked elements, the wavelengths $\Lambda_x$ and $\Lambda_y$ are taken to be equal to the length of the superimposed paired elements (i.e., regular elements with real and additional phantom nodes) in x- and y-directions, respectively. This is because while only part of each superimposed element is used to model one side of the crack, the displacement and pressure fields are interpolated using nodal degrees of freedom located at the nodes on both sides of the crack.**

### *3.2. Mixed GFEM-enriched Phantom Node Method (PNM-GFEM-M)*

The PNM-GFEM approach is extended to the modelling of dynamic transient response of discontinuous porous media, in which discontinuities in both the displacement and pore pressure fields across the fracture surfaces occur. This is accomplished using an approximation analogous to (17) for the pore pressure.

**It is noted that the employed trigonometric enrichment functions in [35] are not exclusively derived for linear elastic case and have been originally proposed in [34] for multi-scale electromagnetic and radio-frequency wave propagation in plasmas. Any type of transient or time-harmonic wave can be represented by exponential (or trigonometric) basis functions based on the Fourier concept and analytical solutions of waves. Hence in [34] the fundamental trig wave functions have been embedded in finite element interpolations as enrichments to mimic the transient/harmonic wave responses. In poroelastic case the response is a combination of diffusion and elastic wave process and the wave-type transient behaviour in displacement field is accompanied by a transient response in pore pressure field. Therefore, there is a coupled transient physics in both displacement and pore pressure variables that can be represented by harmonic functions (i.e., fundamental wave packages).**

As illustrated in Figure 1, the underlying element for our approximation is a mixed element, with a bi-quadratic (nine node) approximation for the displacements and a bi-linear (four node) approximation for the pore pressure. The mixed element is replaced by two superimposed elements: superimposed element 1 (SE1) and superimposed element 2 (SE2). The nodes and corresponding displacement and pressure degrees of freedom of SE1 with $f((X) \leq 0)$ are inherited from the underlining element, while nodes of SE1 with $f((X) > 0)$ are additional phantom nodes with corresponding additional displacement and pressure degrees of freedom. In a similar way, the nodes of SE2 with $f((X) > 0)$ are inherited from the underlining element, while nodes of SE2 with $f((X) \leq 0)$ are additional phantom nodes.

*3.2.1. Displacement field discretization*

For a cracked element in a porous media, the displacement components in $x$ and $y$ directions are interpolated based on the discretization introduced above, in a more compact form as:

$$u_x(x,y,t) = H(-f(x,y)) \sum_{I \in S_1} \left( \boldsymbol{\psi}_I^1(x,y) \boldsymbol{u}_{Ix}(t) \right) + H(f(x,y)) \sum_{I \in S_2} \left( \boldsymbol{\psi}_I^1(x,y) \boldsymbol{u}_{Ix}(t) \right) \tag{18}$$

$$u_y(x,y,t) = H(-f(x,y)) \sum_{I \in S_1} \left( \boldsymbol{\psi}_I^2(x,y) \boldsymbol{u}_{Iy}(t) \right) + H(f(x,y)) \sum_{I \in S_2} \left( \boldsymbol{\psi}_I^2(x,y) \boldsymbol{u}_{Iy}(t) \right) \tag{19}$$

in which $\boldsymbol{\psi}_I^1$ and $\boldsymbol{\psi}_I^2$ are the arrays of conventional and enriched basis functions of node $I$ for the displacement components in $x$ and $y$ directions, respectively. $\mathbf{u}_{Ix}$ and $\mathbf{u}_{Iy}$ are the vectors of corresponding conventional and enriched mixture displacement degrees of freedom of the porous media for node $I$ in the $x$ and $y$ directions, respectively, as shown below.

$$\boldsymbol{\psi}_I^{1,2} = \left[ \begin{array}{cccc} \psi_{I(0,0)} & \psi_{I(1,0)}^{C_x} & \ldots & \psi_{I(n,m)}^{S-} \end{array} \right] \tag{20}$$

$$\boldsymbol{u}_{Ix}^{\top} = [u_{Ix(0,0)}, u_{Ix(1,0)}^{C_x}, ..., u_{Ix(n,m)}^{S-}] \tag{21}$$

$$\boldsymbol{u}_{Iy}^{\top} = [u_{Iy(0,0)}, u_{Iy(1,0)}^{C_x}, ..., u_{Iy(n,m)}^{S-}] \tag{22}$$

The Lagrange interpolation functions ($\psi_{I(0,0)} = N_I$) are taken to be bi-quadratic shape functions ($Q9$).

*3.2.2. Pore pressure field discretization*

When the pore pressure in the cracked element is discontinuous, as when the crack faces are impervious or when the fluid pressure in the fracture is different than in the bulk, pore pressure is approximated by PNM type approximation.

Following the general idea of PNM-GFEM, the pore pressure approximation in discontinuous (pressure) elements is

$$p(x,y,t) = H(-f(x,y)) \sum_{I \in S_1} \left( \boldsymbol{\psi}_I^3(x,y) \boldsymbol{p}_I(t) \right) + H(f(x,y)) \sum_{I \in S_2} \left( \boldsymbol{\psi}_I^3(x,y) \boldsymbol{p}_I(t) \right) \tag{23}$$

in which $\boldsymbol{\psi}_I^3$ denotes the set of conventional and enriched interpolation functions for the pore pressure variable (i.e., the third unknown field of the problem), and $\boldsymbol{p}_I$ is the vector of corresponding regular and enriched, phantom or real pore pressure degrees of freedom for node $I$.

$$\boldsymbol{\psi}_I^3 = \left[ \begin{array}{cccc} \psi_{I(0,0)} & \psi_{I(1,0)}^{C_x} & \cdots & \psi_{I(n,m)}^{S-} \end{array} \right] \tag{24}$$

It is noted that the Lagrange interpolation functions ($\psi_{I(0,0)} = N_I$) for the pore pressure filed are bi-linear shape functions ($Q4$).

*3.3. Semi-discretized mixed FE equations*

Substitution of the prescribed interpolation functions for the displacement fields (18)- (19) and pore pressure field (23) in the governing weak form (14)-(15) results in a semi-discretized system of equations, which at the element level is

$$\sum_{J=1}^{n_{node}} \Big( [M^e]_{IJ}^{11} \ddot{\mathbf{u}}_{Jx}^e + [K^e]_{IJ}^{11} \mathbf{u}_{Jx}^e + [K^e]_{IJ}^{12} \mathbf{u}_{Jy}^e + [K^e]_{IJ}^{13} \mathbf{p}_J^e \Big) = \mathbf{F}_{Iu_x}^e, \quad (I = 1, ..., n_{node}) \tag{25}$$

$$\sum_{J=1}^{n_{node}} \Big( [M^e]_{IJ}^{22} \ddot{\mathbf{u}}_{Jy}^e + [K^e]_{IJ}^{21} \mathbf{u}_{Jx}^e + [K^e]_{IJ}^{22} \mathbf{u}_{Jy}^e + [K^e]_{IJ}^{23} \mathbf{p}_J^e \Big) = \mathbf{F}_{Iu_y}^e, \quad (I = 1, ..., n_{node}) \tag{26}$$

$$\sum_{J=1}^{n_{node}} \Big( [M^e]_{IJ}^{31} \ddot{\mathbf{u}}_{Jx}^e + [M^e]_{IJ}^{32} \ddot{\mathbf{u}}_{Jy}^e + [C^e]_{IJ}^{31} \dot{\mathbf{u}}_{Jx}^e + [C^e]_{IJ}^{32} \dot{\mathbf{u}}_{Jy}^e + [C^e]_{IJ}^{33} \dot{\mathbf{p}}_J^e + [K^e]_{IJ}^{33} \mathbf{p}_J^e \Big) = \mathbf{F}_{Ip}^e, \quad (I = 1, ..., n_{node}) \tag{27}$$

in which $n_{node}$ is the number of nodes in each of the two superposed elements 1 and 2, and includes both original real and phantom nodes. It is noted that for the cracked elements, the numerical integration is performed separately over the active areas of each of the two superposed elements. To evaluate the finite element integrals a sub-domain integration scheme is employed [23].

In an element crossed by a crack, the definitions of $[M^e]_{IJ}$, $[C^e]_{IJ}$, $[K^e]_{IJ}$, $\mathbf{F}_{Iu_x}^e$, $\mathbf{F}_{Iu_y}^e$, and $\mathbf{F}_{Ip}^e$ in (25), (26), and (27) for each of the superimposed elements, i.e., $e$= 1 or 2, are

$$[M^e]_{IJ}^{11} = \int_{A_e} \rho (\boldsymbol{\psi}_I^1)^\top \boldsymbol{\psi}_J^1 d\Omega, \quad [M^e]_{IJ}^{31} = \int_{A_e} \rho_f k_f (\boldsymbol{\psi}_I^3)_{,x}^\top \boldsymbol{\psi}_J^1 d\Omega \tag{28}$$

$$[M^e]_{IJ}^{22} = \int_{A_e} \rho (\boldsymbol{\psi}_I^2)^\top \boldsymbol{\psi}_J^2 d\Omega, \quad [M^e]_{IJ}^{32} = \int_{A_e} \rho_f k_f (\boldsymbol{\psi}_I^3)_{,y}^\top \boldsymbol{\psi}_J^2 d\Omega \tag{29}$$

$$[K^e]_{IJ}^{11} = \int_{A_e} \Big( C_{11} (\boldsymbol{\psi}_I^1)_{,x}^\top (\boldsymbol{\psi}_J^1)_{,x} + C_{33} (\boldsymbol{\psi}_I^1)_{,y}^\top (\boldsymbol{\psi}_J^1)_{,y} \Big) d\Omega, \tag{30}$$

$$[K^e]_{IJ}^{12} = \int_{A_e} \Big( C_{12} (\boldsymbol{\psi}_I^1)_{,x}^\top (\boldsymbol{\psi}_J^2)_{,y} + C_{33} (\boldsymbol{\psi}_I^1)_{,y}^\top (\boldsymbol{\psi}_J^2)_{,x} \Big) d\Omega, \tag{31}$$

$$[K^e]_{IJ}^{13} = \int_{A_e} -\alpha_p (\boldsymbol{\psi}_I^1)_{,x}^\top (\boldsymbol{\psi}_J^3) d\Omega, \tag{32}$$

$$[K^e]_{IJ}^{21} = \int_{A_e} \Big( C_{21} (\boldsymbol{\psi}_I^2)_{,y}^\top (\boldsymbol{\psi}_J^1)_{,x} + C_{33} (\boldsymbol{\psi}_I^2)_{,x}^\top (\boldsymbol{\psi}_J^1)_{,y} \Big) d\Omega, \tag{33}$$

$$[K^e]_{IJ}^{22} = \int_{A_e} \Big( C_{22} (\boldsymbol{\psi}_I^2)_{,y}^\top (\boldsymbol{\psi}_J^2)_{,y} + C_{33} (\boldsymbol{\psi}_I^2)_{,x}^\top (\boldsymbol{\psi}_J^2)_{,x} \Big) d\Omega, \tag{34}$$

$$[K^e]_{IJ}^{23} = \int_{A_e} -\alpha_p (\boldsymbol{\psi}_I^2)_{,y}^\top (\boldsymbol{\psi}_J^3) d\Omega, \tag{35}$$

$$[K^e]^{33}_{IJ} = \int_{A_e} k_f \Big( (\boldsymbol{\psi}^3_I)^\top_{,x} (\boldsymbol{\psi}^3_J)_{,x} + (\boldsymbol{\psi}^3_I)^\top_{,y} (\boldsymbol{\psi}^3_J)_{,y} \Big) d\Omega, \tag{36}$$

$$[C^e]^{31}_{IJ} = \int_{A_e} \alpha_p (\boldsymbol{\psi}^3_I)^\top (\boldsymbol{\psi}^1_J)_{,x} d\Omega, \tag{37}$$

$$[C^e]^{32}_{IJ} = \int_{A_e} \alpha_p (\boldsymbol{\psi}^3_I)^\top (\boldsymbol{\psi}^2_J)_{,y} d\Omega, \tag{38}$$

$$[C^e]^{33}_{IJ} = \int_{A_e} (\boldsymbol{\psi}^3_I)^\top (\boldsymbol{\psi}^3_J) \frac{1}{Q} d\Omega, \tag{39}$$

$$\mathbf{F}^e_{Iu_x} = \int_{A_e} \Big( \rho(b_x) (\boldsymbol{\psi}^1_I)^\top \Big) d\Omega + \int_{s^t_e} \Big( \bar{t}_x (\boldsymbol{\psi}^1_I)^\top \Big) d\Gamma_t + \int_{s^d_e} \Big( \bar{t}_{d_x} (\boldsymbol{\psi}^1_I)^\top \Big) d\Gamma_d, \tag{40}$$

$$\mathbf{F}^e_{Iu_y} = \int_{A_e} \Big( \rho(b_y) (\boldsymbol{\psi}^2_I)^\top \Big) d\Omega + \int_{s^t_e} \Big( \bar{t}_y (\boldsymbol{\psi}^2_I)^\top \Big) d\Gamma_t + \int_{s^d_e} \Big( \bar{t}_{d_y} (\boldsymbol{\psi}^2_I)^\top \Big) d\Gamma_d, \tag{41}$$

$$\mathbf{F}^e_{Ip} = \int_{A_e} k_f \rho_f \Big( (\boldsymbol{\psi}^3_I)^\top_{,x} b_x + (\boldsymbol{\psi}^3_I)^\top_{,y} b_y \Big) d\Omega - \int_{s^w_e} \Big( \dot{w} \cdot n_{\Gamma w} (\boldsymbol{\psi}^3_I)^\top \Big) d\Gamma_w \tag{42}$$

in which $e$ is either 1 or 2 for the superimposed elements one and two, respectively, and $s^t_e$, $s^d_e$, and $s^w_e$ are the portions of superimposed element $e$ on the traction boundary $\Gamma_t$, discontinuity surface $\Gamma_d$, and fluid flux boundary $\Gamma_w$, respectively. $\bar{t}_{d_x}$ and $\bar{t}_{d_y}$ are the components of contact tractions in $x$ and $y$ directions, respectively.

The semi-discretized coupled hydro-mechanical poro-elastic finite element equations (25), (26), and (27) can be rewritten in a more compact form as:

$$[M] \left\{ \ddot{\boldsymbol{\Delta}} \right\} + [C] \left\{ \dot{\boldsymbol{\Delta}} \right\} + [K] \{ \boldsymbol{\Delta} \} = \{ \mathbf{F} \} \tag{43}$$

where $\{\boldsymbol{\Delta}\} = \{ \mathbf{u}_x \;\; \mathbf{u}_y \;\; \mathbf{p} \}^\top$ is the vector of unknown nodal values for displacement and pore pressure degrees of freedom in the porous media, and $\{\mathbf{F}\} = \left\{ \mathbf{F}_{u_x} \;\; \mathbf{F}_{u_y} \;\; \mathbf{F}_p \right\}^\top$ is the vector of mechanical forces and flow fluxes.

### *3.4. Fully Discrete Equations*

To establish the fully-discretized governing algebraic equations, the Generalized Newmark time integration schemes G22 and G11 are employed for displacement and pore pressure degrees of freedom, respectively. The following relations link the unknown values for displacement and pore pressure at time step $(i+1)$ to the corresponding values at time step $(i)$

$$\ddot{u}_{i+1} = \frac{1}{\beta \Delta t^2} (u_{i+1} - u_i) - \frac{1}{\beta \Delta t} \dot{u}_i - (\frac{1}{2\beta} - 1) \ddot{u}_i \tag{44}$$

$$\dot{u}_{i+1} = \frac{\gamma}{\beta \Delta t} (u_{i+1} - u_i) - (\frac{\gamma}{\beta} - 1) \dot{u}_i - \Delta t (\frac{\gamma}{2\beta} - 1) \ddot{u}_i \tag{45}$$

$$\dot{p}_{i+1} = \frac{1}{\theta \Delta t} (p_{i+1} - p_i) - (\frac{1}{\theta} - 1) \dot{p}_i \tag{46}$$

where $\gamma$, $\beta$, and $\theta$ are the integration parameters that are all considered to be 0.7 in the numerical examples of the present work. **The integration constants are typically chosen in the range of [0 1]. For**

**unconditional stability of the time integration $\theta$ and $\gamma$ need to be greater than or equal to 0.5 and $\beta$ should be greater than or equal to $0.25(0.5+\gamma)^2$.**

For a prescribed set of initial and boundary conditions and surface tractions on the crack faces, which may include contributions from friction and contact forces, the substitution of (44-46) into (43) leads to a linear system of equations of the following form for the displacement and pressure degrees of freedom $\boldsymbol{\Delta}_{i+1}$ at time $t_{i+1}$ in terms of known displacement and pressure degrees of freedom $\boldsymbol{\Delta}_i$ at time $t_i$.

$$\mathbf{A}\boldsymbol{\Delta}_{i+1} = \mathbf{R}\left(\boldsymbol{\Delta}_i, \bar{\mathbf{t}}, \bar{\mathbf{t}}_d, \bar{\mathbf{q}}\right) \tag{47}$$

in which the right hand side $\mathbf{R}$ is function of the degrees of freedom at time $t_i$, the external applied traction $\bar{\mathbf{t}}$, the crack surface tractions $\bar{\mathbf{t}}_d$, and the boundary flux $\bar{\mathbf{q}} = \dot{\boldsymbol{w}} \cdot \boldsymbol{n}_\Gamma$. In the next section, the calculation of the crack surface tractions stemming from friction and contact is discussed.

## 4. Augmented-Lagrangian frictional contact simulation

Geomechanical porous systems experience high in-situ confining stresses due to the overburden and horizontal stresses leading to large contact and frictional forces acting along natural fractures and faults. A considerable amount of attention has been given to how to enforce interfacial constraints in the context of the partition-of-unity FEM; a number of contact simulation methodologies and appropriate spacial and interfacial interpolation strategies have been developed leading to smoother and more stable contact results [30, 31, 32, 33]. In this work, an augmented Lagrange multiplier approach is adopted to enforce the normal contact constraint via an iterative method.

When frictional contact between crack surfaces is incorporated into the model, it is convenient to rewrite the weak form (14) as

$$\int_\Omega \boldsymbol{\sigma} : \delta\boldsymbol{\varepsilon}\; d\Omega + \int_\Omega \rho\ddot{\boldsymbol{u}} \cdot \delta\boldsymbol{u}\; d\Omega - \int_{\Gamma_t} \bar{\boldsymbol{t}} \cdot \delta\boldsymbol{u}\; d\Gamma - \int_\Omega \rho\boldsymbol{b} \cdot \delta\boldsymbol{u}\; d\Omega - \int_{\Gamma_d} \bar{\lambda}_N g_N d\Gamma -$$

$$\int_{\Gamma_d} \bar{\lambda}_T g_T d\Gamma = 0 \tag{48}$$

in which $\bar{\lambda}_N$, $g_N$, $\bar{\lambda}_T$, and $g_T$ are the normal contact traction, the normal inter-penetration, the tangential contact frictional traction, and the tangential displacement jump across the contact surface, respectively. It is noted that the inter-penetration ($g_N$) has been defined with a positive sign. Here $\bar{\lambda}_T$ is the friction stemming for a stick-slip friction model.

The normal contact and tangential frictional force/Lagrange multiplier fields are interpolated using one-dimensional elements along the discontinuity as:

$$\bar{\lambda}_N = \tilde{\mathbf{N}}\bar{\boldsymbol{\lambda}}_N \text{ and } \bar{\lambda}_T = \tilde{\mathbf{N}}\bar{\boldsymbol{\lambda}}_T \tag{49}$$

in which $\tilde{\mathbf{N}}$ are linear one-dimensional Lagrangian shape functions and $\left(\bar{\boldsymbol{\lambda}}_N, \bar{\boldsymbol{\lambda}}_T\right)$ are the vectors of Lagrange multipliers degrees of freedom. The nodes of the Lagrange multiplier mesh are chosen using the Vital Vertex Method [31, 32].

At each time step, $\boldsymbol{\Delta}_{i+1}$ and $\left(\bar{\boldsymbol{\lambda}}_N, \bar{\boldsymbol{\lambda}}_T\right)_{i+1}$, given the solutions $\boldsymbol{\Delta}_i$ and $\left(\bar{\boldsymbol{\lambda}}_N, \bar{\boldsymbol{\lambda}}_T\right)_i$ at $t_i$, are sought using an iterative process. The iterative process starts ($k=0$) with an initial guess for the vector of Lagrange multipliers $\left(\bar{\boldsymbol{\lambda}}_N, \bar{\boldsymbol{\lambda}}_T\right)_{i+1}^{k=0} = \left(\bar{\boldsymbol{\lambda}}_N, \bar{\boldsymbol{\lambda}}_T\right)_i$. Given $\left(\bar{\boldsymbol{\lambda}}_N, \bar{\boldsymbol{\lambda}}_T\right)_{i+1}^{k}$ at iteration $k$, the linear system of equations (47) is solved for $\boldsymbol{\Delta}_{i+1}^k$, from which the normal interpenetration $g_N^k$ and tangential slip $g_T^k$ of the crack at each node of the Lagrange multiplier mesh are computed. If the norm of $g_N^k$ is greater than a prescribed tolerance then the Lagrange multiplier nodal vector (normal contact forces) are updated using

$$\bar{\boldsymbol{\lambda}}_N^{k+1} = \bar{\boldsymbol{\lambda}}_N^k + d\bar{\boldsymbol{\lambda}}_N^k, \quad \textit{and} \quad d\bar{\boldsymbol{\lambda}}_N^k = K_N g_N^k \tag{50}$$

Table 1: Material properties of the porous media.

| $E(Pa)$ | $\nu$ | $\rho_s(kg/m^3)$ | $\rho_f(kg/m^3)$ | $n'$ | $k_f(m^3s/kg)$ | $K_f(Pa)$ | $K_s(Pa)$ |
|---|---|---|---|---|---|---|---|
| $14.516 \times 10^6$ | 0.3 | 2000 | 1000 | 0.3 | $1.0194 \times 10^{-6}$ | $2.1 \times 10^9$ | $1 \times 10^{20}$ |

in which $K_N$ is an arbitrary rebounding stiffness value.

In the case of frictional contact, a similar iterative update procedure is implemented to obtain the frictional (i.e., tangential) contact nodal forces. Sliding occurs, $g_T > 0$, if the tangential frictional contact force, $\bar{\lambda}_T$, required to prevent slip exceeds $\bar{\lambda}_T^{max} = \bar{\lambda}_N \mu_f$, otherwise a state of stick exists and the associated tangential slip, $g_T$, should be 0. When frictional contact is modelled, the iterative process is also conditioned on the norm of the tangential slip $g_T$ at Lagrange multiplier nodes in a state of stick being less than a prescribed tolerance. When this condition is not satisfied, the Lagrange multiplier nodal vector associated with the stick-slip friction is updated using

$$\begin{cases} \bar{\boldsymbol{\lambda}}_T^{k+1} = \bar{\boldsymbol{\lambda}}_T^{k} + K_T g_T^k & \text{if } \bar{\lambda}_T < \bar{\lambda}_T^{max,k+1} \quad \text{(Stick Condition)} \\ \bar{\boldsymbol{\lambda}}_T^{k+1} = \bar{\lambda}_T^{max,k+1} & \text{otherwise} \qquad\quad \text{(Slip Condition)} \end{cases} \tag{51}$$

in which $\bar{\lambda}_T^{max,k+1} = \bar{\lambda}_N^{k+1} \mu_f$ and $K_T$ is an arbitrary rebounding stiffness.

By repeating the iterative process at each time step, the normal inter-penetration at the crack location approaches zero as the vector of Lagrange multiplier, $\bar{\lambda}_N^{k+1}$, converges to the real magnitude of the contact force at the interface of the crack. In a similar way, the frictional contact forces converge to those satisfying the stick-slip condition. Once convergence of the iterative procedure is achieve, the solution algorithm proceeds to the next time step.

## 5. Results and discussion

In this section, different types of dynamic and transient wave propagation problems are simulated in poroelastic domains. The domain of analysis is assumed to be a two-dimensional poroelastic media with hydro-mechanical properties given in Table 1, unless stated otherwise. A unit thickness is assumed in the out-of-plane direction.

### *5.1. Verification study - Consolidation*

To verify the accuracy and reliability of the developed enriched finite element model in solving dynamic transient poroelastic problems, the results obtained using the enriched FE model of the present work (with $n = 1$) is compared with some available results from the literature. To this end, **as shown schematically in Figure 2** a vertical column of small width is considered under uniformly applied external traction on its top surface. The side walls and the bottom are assumed to be impervious and there is normal displacement restriction on them. The upper boundary is drained ( there is essential boundary condition for p, i.e., p=0 ) and under compressive normal uniform traction of 3 $kN/m^2$. The width and length of the porous column are $0.1m$ and $10m$, respectively, and a one dimensional coordinate system is set on the domain with its origin at the bottom of the vertical column. **Sixty rectangular $Q4$ elements with bi-linear polynomial interpolations have been considered to model this problem**. Figures 3 and 4 show the velocity and pore pressure time histories of the transient response in the domain for particular control points on the column. As seen in these figures, a very close agreement is observed between the results of the numerical model of this work and those reported in [8].

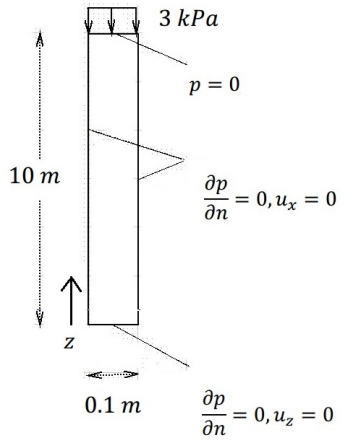


Figure 2: A schematic picture of the porous column used for the validation study.

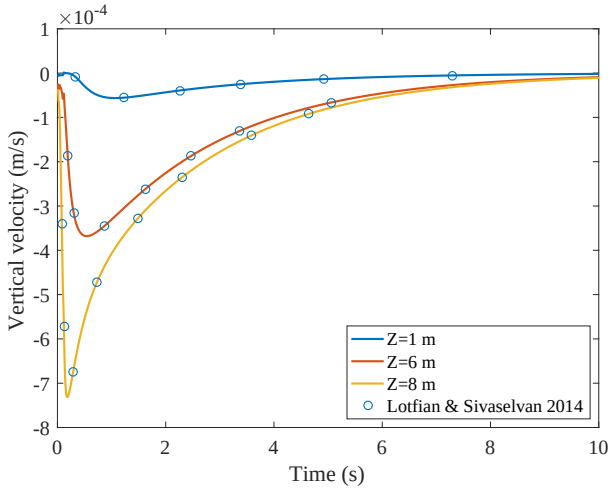


Figure 3: A comparison study of the proposed enriched FE model with [8] on the variation of point velocity over time for vertical column of porous media.

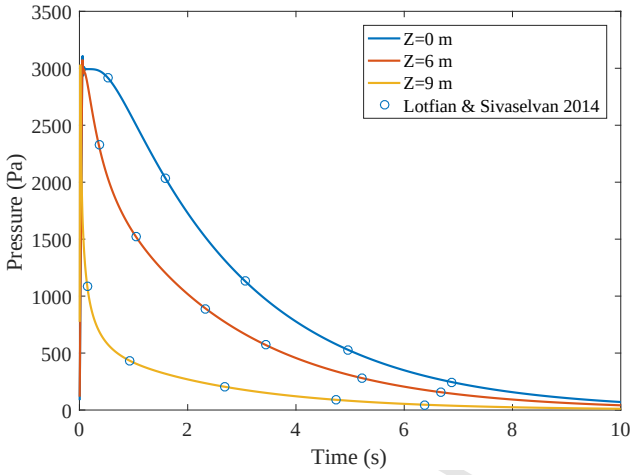


Figure 4: A comparison study of the proposed enriched FE model with [8] on the variation of pore pressure over time for vertical column of porous media.

*5.2. Dynamic response of fractured porous media under external traction-*

To investigate the effect of discontinuity on the dynamic response of porous media, a $1m \times 0.1m$ poroelastic domain discretized by $30 \times 10$ $Q4$ mesh is considered. The domain contains a vertical crack of length $0.06m$ centered at $x = 0.5m$. The crack faces are assumed to be hydraulically impervious. Simulations with and without crack surface contact are modeled and are compared to the case of a continous intact domain. A uniform traction is imposed on the left side of the domain ($x = 0$) as:

$$\bar{t}_x(t) = \begin{cases} 3000 \times \frac{t}{0.1}[N/m^2] & \text{if } t \leqslant 0.1s; \\ 3000 & \text{if } t > 0.1s. \end{cases} \tag{52}$$

The top, bottom, and right edges of the domain are assumed to be impervious and the normal displacements to these edges are constrained. The left edge of the domain is fully drained. The domain, crack geometry, and the boundary conditions are shown in Figure 5.

**In this problem long term dynamic response is investigated, which is comprised of lower frequency components. This is in contrast with the early time dynamic response, which is comprised of higher frequency components. In the case of the former long term dynamic behaviour, the regular (uneriched) PNM model can be employed to accurately model the porous media.**

Figure 6a illustrates the x-displacement contour of fractured domain at $t = 0.16$ $s$ when contact between the crack faces is modeled. As seen in this contour plot, the contact no-interpenetration constraint is satisfied across the crack faces. On the other hand, as expected, neglecting the contact condition along the fracture faces results in a discontinuous displacement field, results for which are shown in Figure 6b. Neglecting the contact traction results in a higher magnitude of peak displacement in the field compared to the case in which the contact problem is accounted for. **Figure 6c illustrates the differences between the response of the fractured porous media along the center-line, $y = 0.05$, with and without contact modeled along the crack faces. When contact is modeled the displacements normal to the crack are continuous, whereas when contact is not modeled the displacements are discontinuous across the crack.**

**Figures 7a, 7b, and 8 illustrate, respectively, the pore fluid velocity contour in x-direction, pore fluid velocity streamlines, and normal strain in the x-direction ($\varepsilon_{xx}$) at $t = 0.08s$ using $90 \times 60$ $Q4$ mesh. As seen in Figures 7a and 7b, because of the existence of an impervious crack, the streamlines go around the fracture and the velocity of the fluid perpendicular to the fracture**

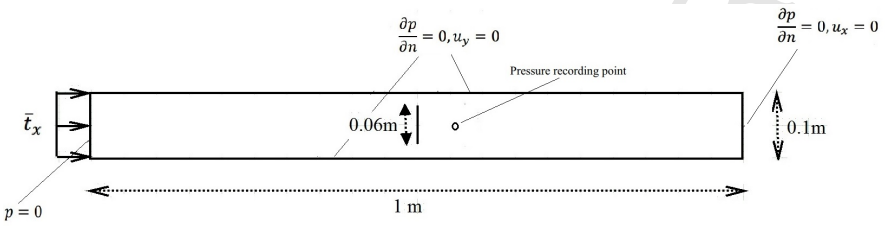


Figure 5: A schematic figure of the porous media of section 5.2.

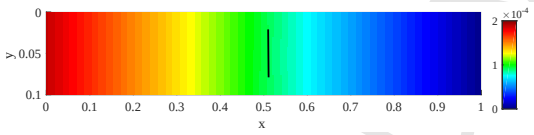

(a) with contact traction along crack faces

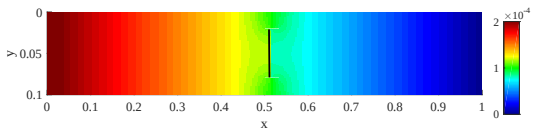

(b) with no contact traction along crack faces

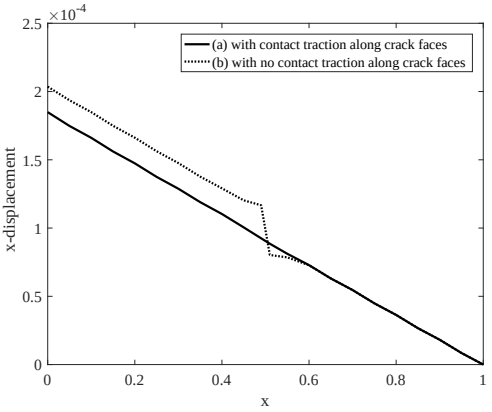


(c) 2D plot of x-displacement along the center-line (i.e., y=0.05)

Figure 6: x-displacement under external uniformly distributed loading on the left edge at ($t = 0.16\ s$).

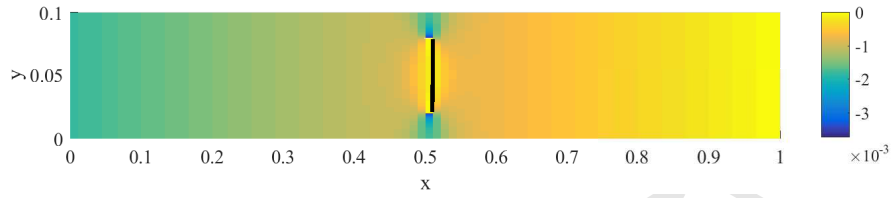


(a) Velocity contour in x-direction.

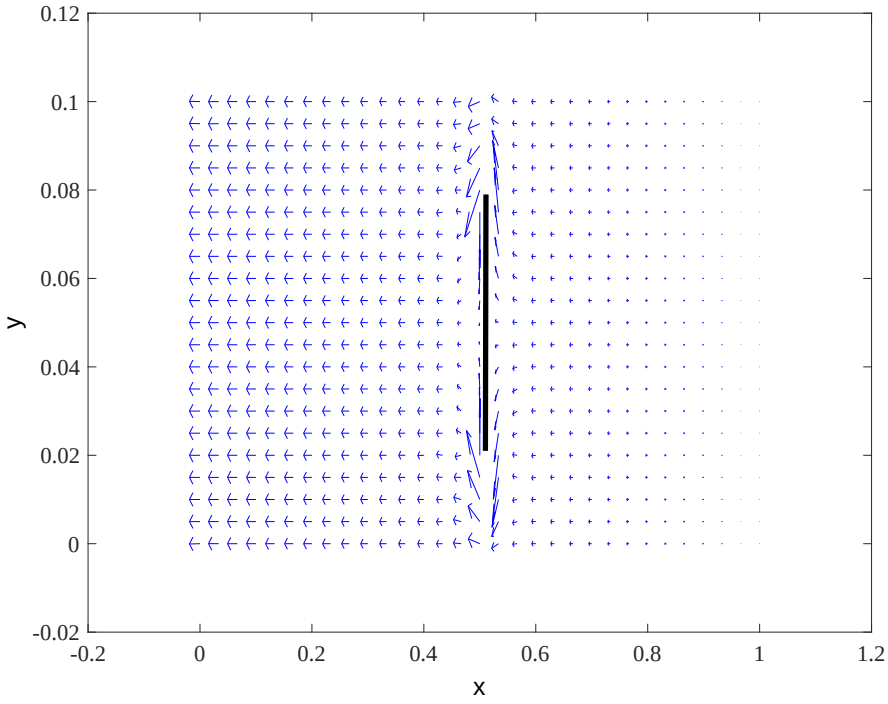


(b) Velocity streamlines.

Figure 7: Pore fluid velocity at $t = 0.08s$.

**at the interface of the discontinuity is zero (no fluid flux goes through the fracture). As seen in Figure 8 the strain magnitude at the fracture surface region is zero due to the traction-free interface assumption.**

To further demonstrate the effect of the existence of crack on the hydraulic response of porous media, Figures 9a and 9b illustrate the pore pressure distribution through the fractured and intact domain, respectively. In the case of fractured domain it was assumed that the crack faces were completely impervious. As seen, the discontinuity in the pore pressure across the fracture is clear in Figure 9b while Figure 9a exhibits a continuous distribution for pore pressure. Moreover, due to the impermeability of crack faces, the maximum pore pressure of the domain (behind the crack) is higher than that of the intact media with no crack after the pore fluid begins to be discharged from the domain through the drained surface (left edge). This phenomenon happens due to the trapping of the pore fluid behind the fracture in the discharge process which makes the fluid discharge slower compared to the case with no crack. Figure 10 shows the time history of the pore pressure at a particular point in the domain ($x = 0.5667\ m, y = 0.05\ m$) behind the fracture. The impermeability of crack faces results in higher peak pressure in the cracked domain compared to the

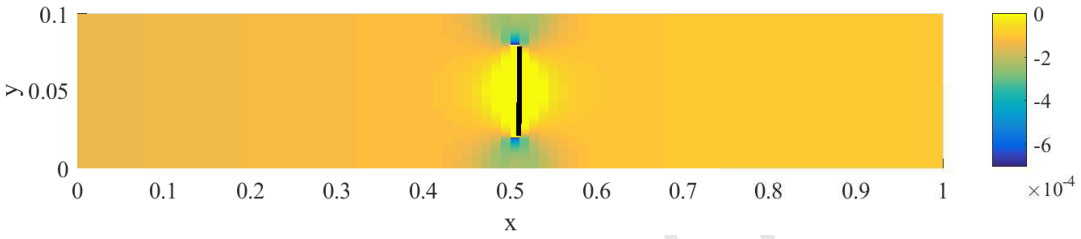


Figure 8: Strain contour ($\varepsilon_{xx}$) at $t = 0.08s$.

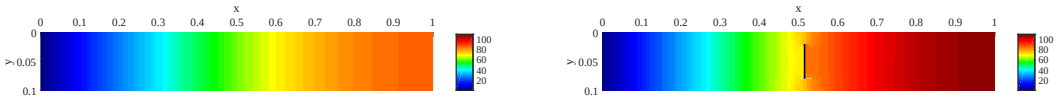

(a) Intact domain with no fracture

(b) Fractured domain with contact

Figure 9: Pore pressure distribution under external uniformly distributed loading on the left edge at ($t = 0.16$ $s$).

intact media. Due to the existence of drained hydraulic boundary condition at the left edge, as the system moves forward the pore pressure gradually tends to zero in steady state condition.

### *5.3. Dynamic response of fractured porous media under point injection*

To investigate the transient response of fractured porous media under hydraulic stimulation, a $1m$ by $1m$ domain (illustrated schematically in Figure 11) is considered under point injection at the center of the domain. The system is discretized by a $10 \times 10$ $Q4$ rectangular mesh. The boundaries are fully drained and are assumed to be traction-free with no displacement constraints. The problem is solved for the cases of discontinuous and intact domain. For the case of discontinuous media a vertical crack of $0.6m$ length is embedded at $x = 0.65m$. The problem is investigated under impervious as well as permeable crack face conditions. Contact constraints are considered for the cases in which there exists a crack. Due to the diffusive nature of this hydraulically-stimulated problem, regular PNM is used for the simulation.

To asses the effect of the hydraulic loading rate on the dynamic response of the system, two types of point injection rates are considered as:

- Case 1 (rapid injection):

$$\bar{q}(t) = \begin{cases} 0.01 \times \frac{t}{1\times10^{-4}}[m^3/s] & \text{if } t \leqslant 1 \times 10^{-4}s; \\ 0.01 & \text{if } t > 1 \times 10^{-4}s. \end{cases} \tag{53}$$

- Case 2 (slow injection):

$$\bar{q}(t) = \begin{cases} 0.01 \times \frac{t}{100\times10^{-4}}[m^3/s] & \text{if } t \leqslant 100 \times 10^{-4}s; \\ 0.01 & \text{if } t > 100 \times 10^{-4}s. \end{cases} \tag{54}$$

Figures 12a and 12b illustrate the early responses of the pore pressure at the mid-point of the domain as a function of time for two different injection rates into fractured and intact (continuous) domains. For the case of rapid injection, a peak-pressure point exist in the pore pressure time history. After the peak-pressure, the pore pressure abruptly drops-off before gradually increasing to a steady-state value. The pressure peak in the high injection rate simulation are a result of the initially undrained behaviour of the porous media. In contrast, under slow injection the pore pressure increases in a nearly monotonically way towards a steady-state. The pore pressure response of an intact domain under both rapid and slow injection are also illustrated in Figures 12a and 12b. In both cases, the pore pressure response of the intact domain falls beneath that of the fractured domain. This behaviour is reasonable, since the cracks were assumed to be impervious and so the effective hydraulic conductivity of the fractured domain is less than that of the intact

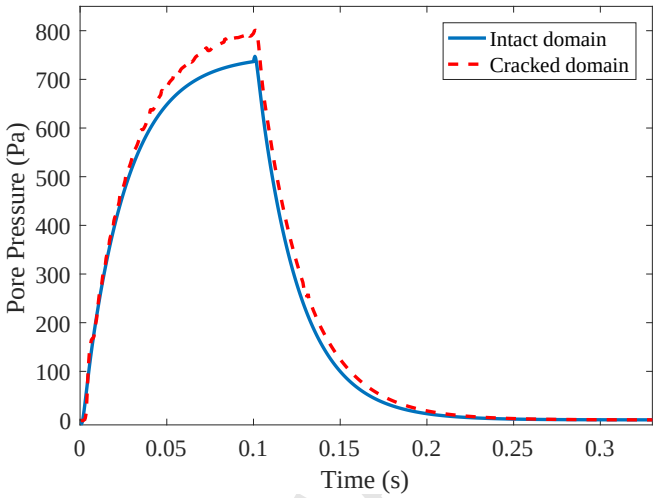


Figure 10: Time history of pore pressure at point ($x = 0.5667\ m, y = 0.05\ m$) for cracked and intact domains.

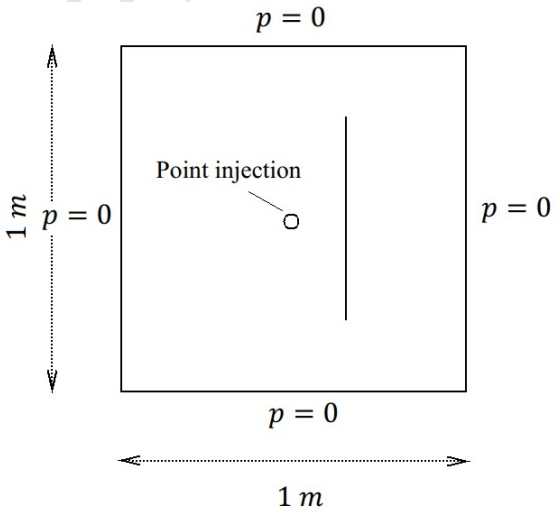


Figure 11: Schematic picture of porous media under point injection.

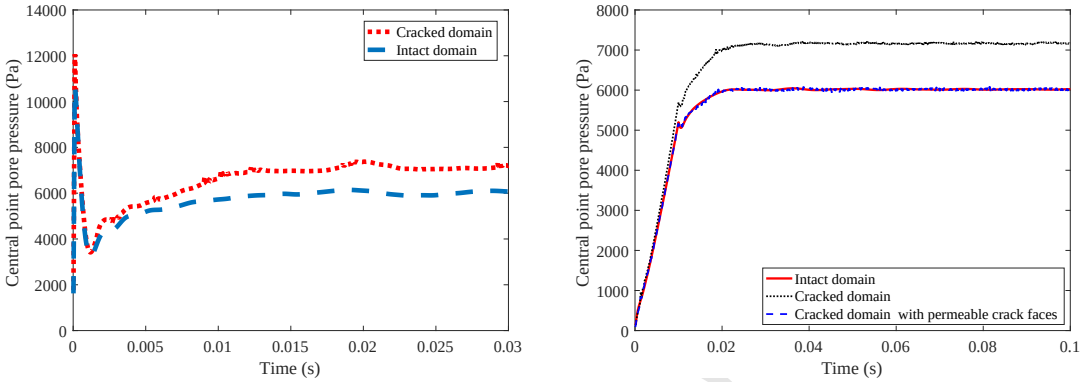


(a) Case 1 point injection (rapid injection)

(b) Case 2 point injection (slow injection)

Figure 12: Pore pressure time history under point injection.

(continuous) domain. As a means to further verify the PNM and contact implementations, the simulated hydraulic response of the fractured media with fully-permeable crack surfaces is also included in Figure 12b. The responses of the fractured media with fully-permeable crack surfaces and contact is almost identical to that of intact domain, as would be expected.

### *5.4. Dynamic response under point injection in porous media with multiple fractures*

To demonstrate the applicability of the developed model in hydro-mechanical simulation of porous media with multiple fractures, Figure 13 exhibits the pore pressure contour of a domain with three cracks as shown in the figure. The domain is considered to be under Case 2 type of point injection as represented in the preceding example in section 5.3. In the example PNM is used to introduce impermeable fractures. The domain is discretized by a $20 \times 20$ $Q4$ rectangular mesh. To specify the geometry of the fractures of this model the starting and finishing points of the cracks are given. For the vertical crack: $(x_{starting} = 0.3m, y_{starting} = 0.2m)$ and $(x_{finishing} = 0.3m, y_{finishing} = 0.8m)$; for the first sloping crack: $(x_{starting} = 0.5m, y_{starting} = 0.1m)$ and $(x_{finishing} = 0.67m, y_{finishing} = 0.4m)$; and for the second sloping crack: $(x_{starting} = 0.67m, y_{starting} = 0.6m)$ and $(x_{finishing} = 0.5m, y_{finishing} = 0.9m)$. Figure 13 shows a snapshot of pore pressure distribution at $t = 0.055s$. As expected, the figure shows a discontinuous distribution for the pore pressure due to the impermeability assumption on crack faces.

### *5.5. Stick-slip frictional contact behaviour of fractured porous media*

To examine the ability of the developed FE model to simulate frictional contact phenomenon in porous media a $1m \times 0.1m$ domain with a tilted crack is considered, as schematically shown in Figure 14. The crack faces are assumed to be impervious. A time dependent traction of the following form is applied on the left side ($x = 0$) of the domain.

$$\bar{t}_x(t) = \begin{cases} 3000 \times \frac{t}{0.1}[N/m^2] & \text{if } t \leqslant 0.1s; \\ 3000 & \text{if } t > 0.1s. \end{cases} \tag{55}$$

Top, bottom, and right boundaries are assumed to be impervious and normal displacements are restricted. The left edge is hydraulically open. **In this problem long term dynamic response is investigated, which is comprised of lower frequency components. This is in contrast with the early time dynamic response, which is comprised of higher frequency components. In the case of the former long term dynamic behaviour, the regular (uneriched) PNM model can be employed to accurately model the porous media.**

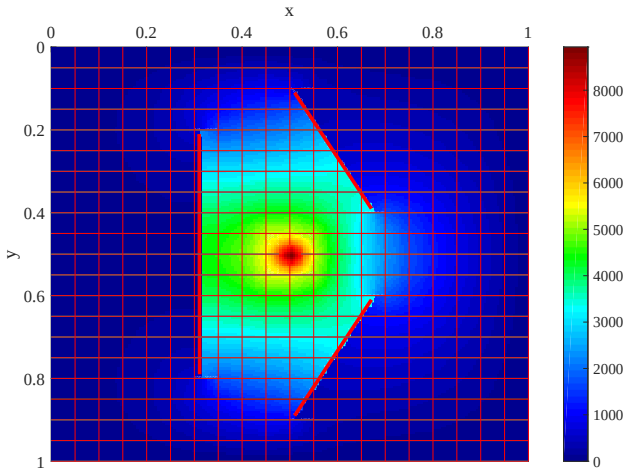


Figure 13: Pore pressure distribution under point injection at $t = 0.055s$ in porous media with multiple fractures.

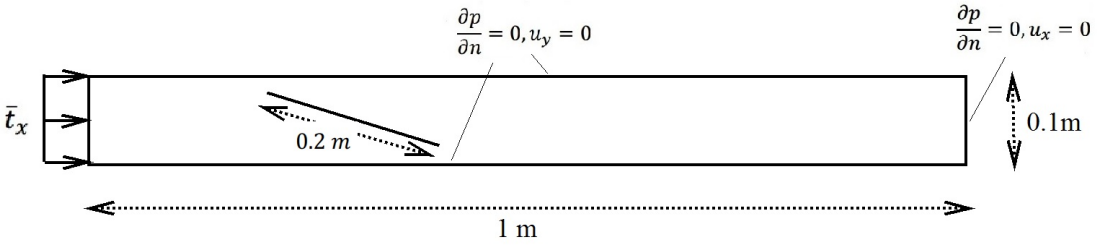


Figure 14: Schematic picture of porous media with inclined crack.

To simulate different frictional contact behaviour, from full-slip to perfect-stick conditions, four different friction coefficients of $\mu_f = 0.00$, $\mu_f = 0.05$, $\mu_f = 0.10$, and $\mu_f = 0.50$ are examined. Results for each of these coefficients are shown in Figures 15a, 15b, 15c, and 15d, respectively. **Figure 15e shows the variation of x-displacements as a function of $x$ along the center-line (i.e., $y = 0.05$) for different friction coefficients. As the friction coefficient increases the magnitude of the displacement discontinuity decreases.** As can be observed, by increasing the friction coefficient magnitude from 0 to 0.5, the contact behaviour of the system changes from the condition of fully-slip to perfect-stick response.

### *5.6. Wave propagation in porous media: Regular vs enriched FE*

In this section the ability of the proposed PNM-GFEM-M model in simulating transient wave propagation is assessed for the case of velocity impact problem in continuous and fractured porous media. The results are compared with regular FEM/PNM simulations to demonstrate the capability of the developed enriched FE model in suppressing the high-frequency spurious oscillations in both displacement and pore pressure variables. **In the numerical simulations of this section, bi-quadratic ($Q9$) and bi-linear ($Q4$) polynomials are used as shape functions for interpolation of the displacement and pore pressure fields, respectively.**

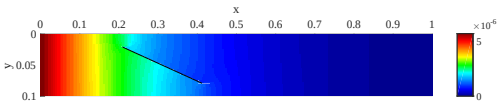

(a) $\mu_f = 0.00$ (no friction- slip behaviour)

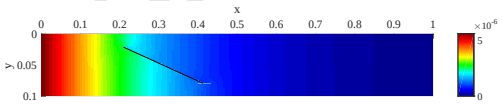

(b) $\mu_f = 0.05$ (stick-slip behaviour)

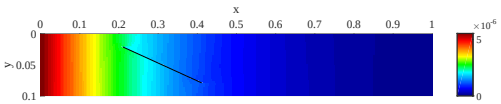

(c) $\mu_f = 0.10$ (stick-slip behaviour)

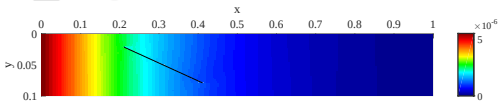

(d) $\mu_f = 0.50$ (stick behaviour)

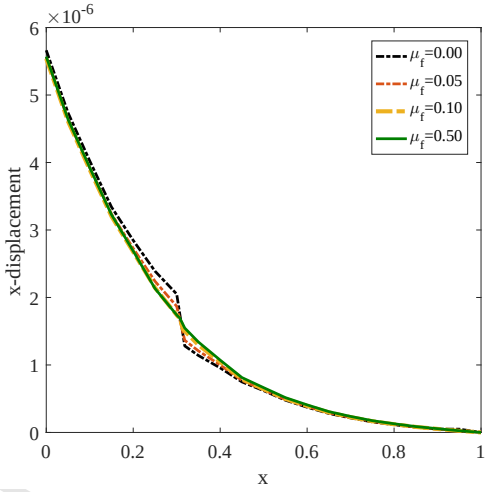


(e) 2D plot of x-displacement along the center-line (i.e., y=0.05)

Figure 15: x-displacement under frictional contact.

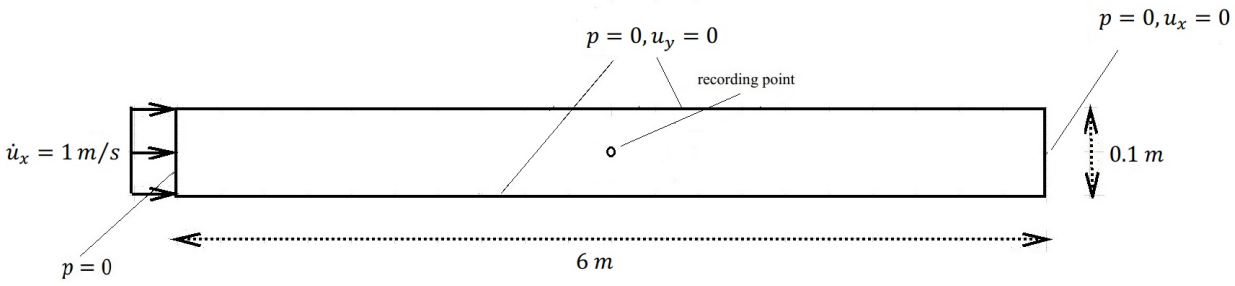


Figure 16: Schematic picture of porous media under velocity impact loading.

*5.6.1. Impact problem in continuous media*

The fixed-velocity impact phenomenon is known to be a good benchmark problem to examine the accuracy of a developed finite element method for wave propagation[35]. To demonstrate the ability of the developed enriched finite element model in solving the problem of transient wave propagation in porous media a poroelastic domain of $6m \times 0.1m$ is considered. An impact mechanical load is applied on the left edge of the domain and is imposed in the form of a fixed velocity boundary condition of $\dot{u}_x = 1m/s$. All the boundaries are considered to be fully-drained and with displacement restrictions normal to the domain. The considered domain, the boundary conditions, and the loading are exhibited schematically in Figure 16.

**The impact problem investigated here is similar to the benchmark problem for evaluating the accuracy of dynamic finite element analysis for non-porous media [35]. In the case of non-porous media, it is known that the velocity response is a step function with no oscillations. In the case of porous media, we are not aware of the existence of an analytical solution for this problem. However, it's expected that the velocity response of the solid matrix will be similar to the non-porous media case, but that the response will be a step-like function with a steep but non-infinite slope. The slope of the step-like function is expects to decrease as the wave propagates due to diffusion of the fluid in the porous media. The expected behaviour of the pore pressure is also non-oscillatory. The compressive wave in displacement/velocity field stimulates pore pressure at the wave front. The induced pore pressure at the velocity front is then expected to decay over time due to diffusion. Hence, it is physically sensible to see a moving pulse, free from oscillations in the pore pressure during the wave propagation.**

For a $20 \times 2$ mesh, Figures 17 and 18 illustrate the time histories at the center of the domain at ($x = 3m$, $y = 0.05m$) for x-velocity and pore pressure, respectively. Comparing the results of conventional/unenriched FEM with those obtained using the GFEM model of this work demonstrates the shortcoming and deficiency of regular/conventional FE models and also, the requirement for employing enriched/unconventional finite element models for wave propagation analysis of porous media. As can be seen in both figures, the velocity and pore pressure curves exhibit high-frequency non-physical spurious oscillations over time in the case of conventional FEM. However, the oscillations (numerical dispersions that appear due to the Gibb's phenomenon) can be significantly suppressed by employing the GFEM model. In other words, using the GFEM model for porous media results in much more accurate wave patterns in both velocity and pore pressure fields. In Figure 17 it can be observed that using the GFEM model leads to a velocity-time profile that is very close to the step-function response, which is the analytical solution of this impact problem.

It is very important to note that in Figure 18 the results of the GFEM model have been provided for different types of enrichments for the displacement field ($u$) and pore pressure field ($p$). As seen in this figure, the most accurate results for pore pressure wave pattern are obtained when both displacement and pressure fields are enriched using trigonometric basis function in the context of GFEM. The GFEM models that are enriched only in the displacement field exhibit relatively more oscillations compared to the GFEM models that are enriched for both displacement and pore pressure. Moreover, increasing the cutoff number of enriched basis functions embedded in the GFEM model leads to the wave results with fewer spurious oscillations and subsequently to more accurate solutions. Figure 19 shows the wave propagation results of pore

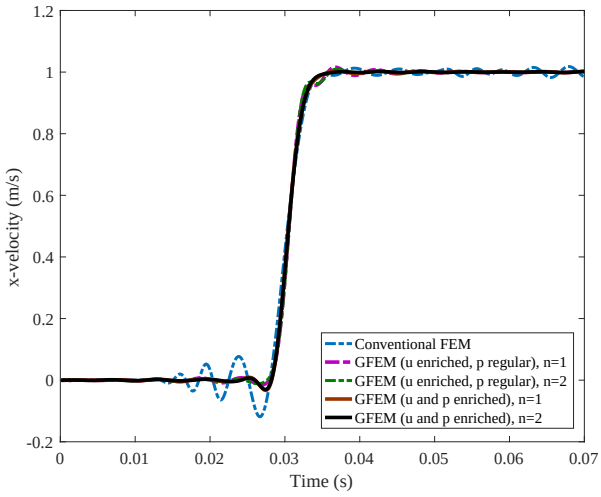


Figure 17: Time history for x-velocity at the mid point of the porous media under impact loading. Conventional FEM Vs the developed GFEM model of this work with different types of enrichment for displacement and pore pressure fields.

pressure for a longer period of time. In this case, the effect of wave reflection from boundaries are observed. As seen, when using the conventional FEM model the non-physical oscillations exist for primary emitted wave (the very first pulse) as well as the waves reflected from the boundaries (the second pulse onward). The effect of physical damping/dissipation (which is attributed to the viscous pore fluid) is apparent from the attenuation of the pressure pulse as the wave travels. Also it is observed that the spurious oscillations tend to gradually subside over time due to this attenuation.

**Figure 20 demonstrates a convergence study of regular FE approach for the impact problem. Different mesh resolutions are considered to simulate the wave propagation response. As seen, the conventional FEM approach shows noticeable numerical dispersions and oscillations even for highly refined meshes. However, the refined regular finite element solutions are converging (qualitatively) to enriched finite element result (see Figure 18). In Figure 20 the regular FEM model with the highest mesh resolution ($400 \times 2$ elements) has 12015 degrees of freedom while in Figure 18 the GFEM model with the coarsest mesh resolution ($20 \times 2$ elements with $n = 1$) has 1435 degrees of freedom. Although the number of degrees of freedom in regular FEM simulation is more than 8 times higher than that of the enriched GFEM model, the enriched model provides more accurate (spurious oscillation-free) results. Moreover, the computational cost of the simulation using the mentioned enriched GFEM model is proportionally lower than that of the regular FEM simulation.**

*Role of Permeability*

To assess the effect of the permeability parameter on wave propagation response of porous media, Figure 21 shows the pore pressure time history of the same problem for a lower permeability/diffusivity porous media case ($K_f = 1.0194 \times 10^{-7}$). As seen, lower values for permeability results in higher peak pore pressures. Moreover, regular FE analysis of porous media with lower permeability shows even relatively less oscillations compared with the preceding case with $K_f = 1.0194 \times 10^{-6}$ since the hydraulic behaviour is closer to undrained, as the permeability decreases.

To have a better intuitive understanding to the effect of permeability on transient wave propagation response of porous media, Figures 22 through 25 show the wave propagation responses for pore pressure and velocity variables at the mid point of the media for various values of permeability. Comparing the figures

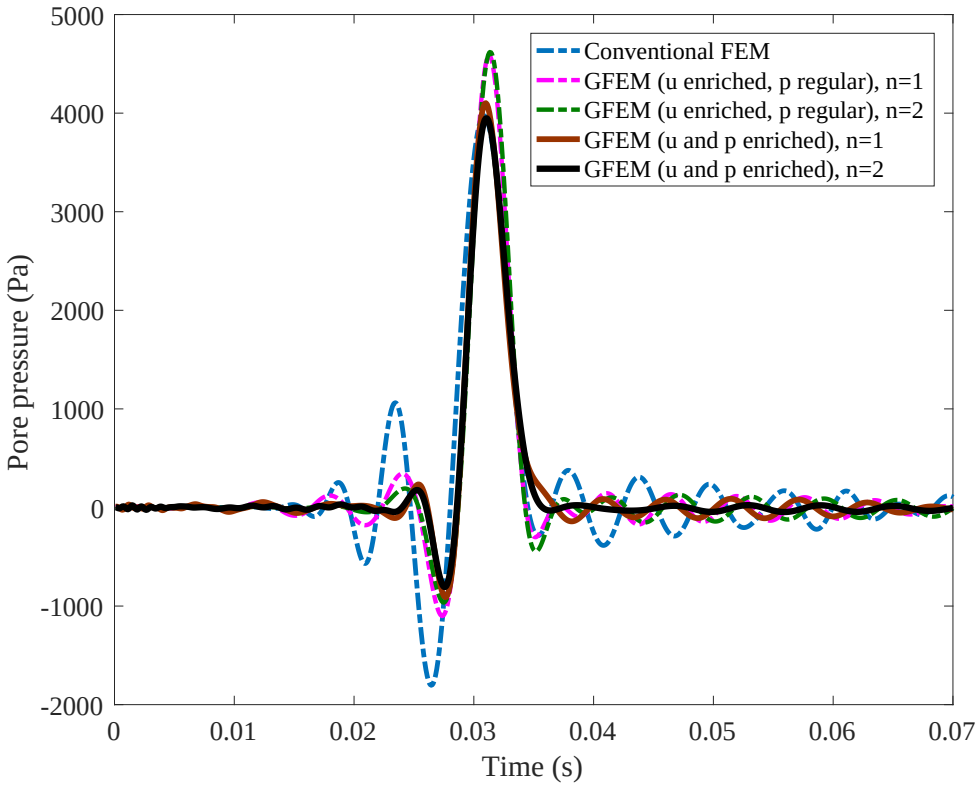


Figure 18: Time history for pore pressure at the mid point of the porous media with $K_f = 1.0194 \times 10^{-6}$ under impact loading. Conventional FEM Vs the developed GFEM model of this work with different types of enrichment for displacement and pore pressure fields.

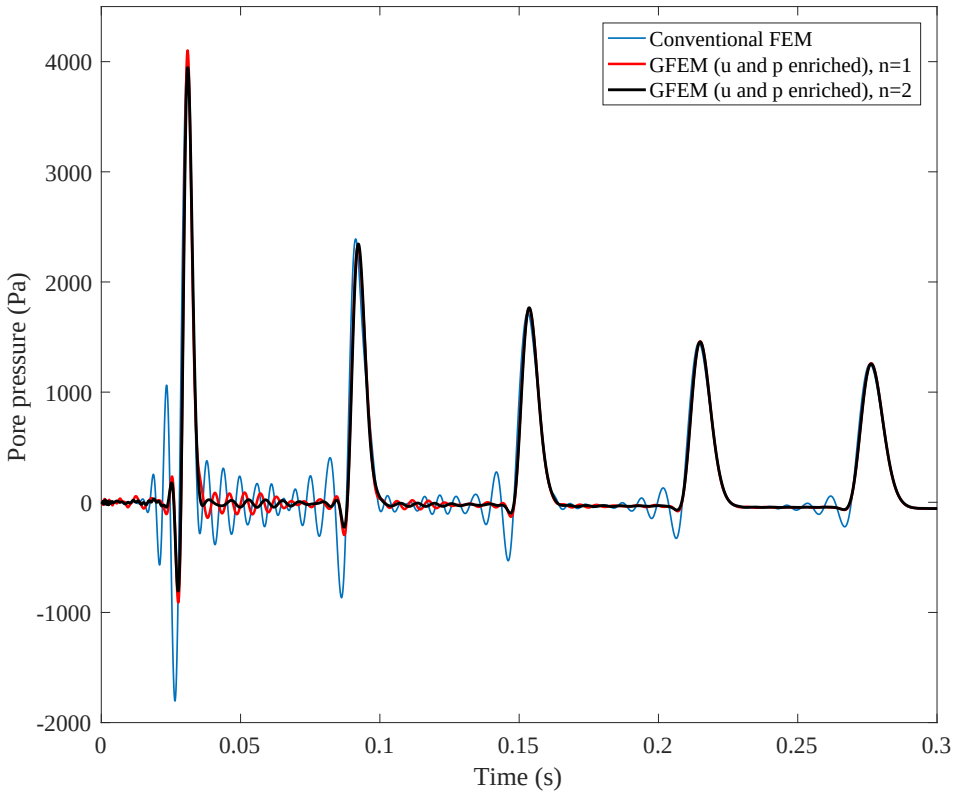


Figure 19: Time history of pore pressure at the mid point of the porous media under impact loading with wave reflection from the boundaries. Conventional FEM Vs the developed GFEM model of this work.

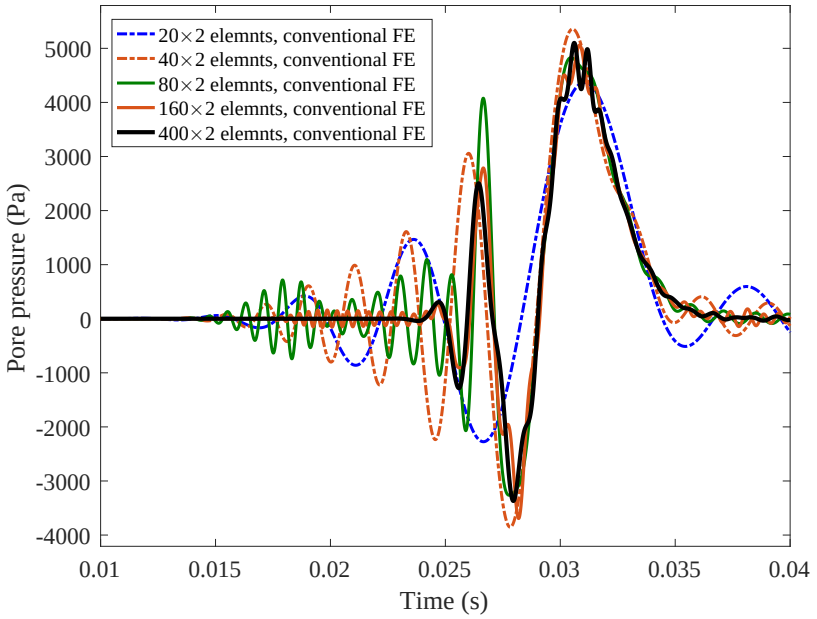


Figure 20: Convergence study of conventional FE approach for pore pressure at the mid point.

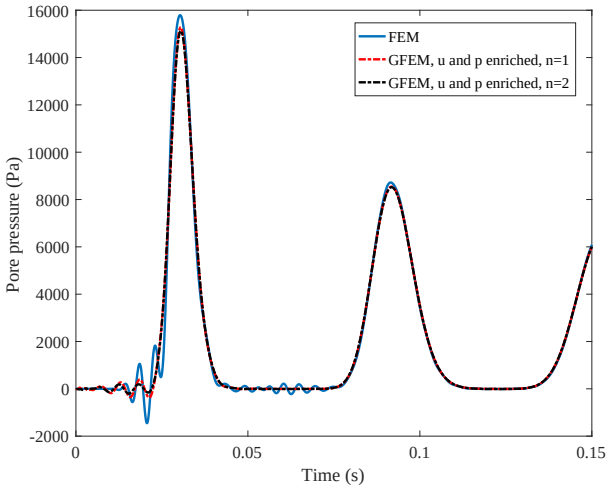


Figure 21: Time history of pore pressure at the mid point of the porous media under impact loading with wave reflection from the boundaries with $K_f = 1.0194 \times 10^{-7}$. Conventional FEM Vs the developed GFEM model of this work.

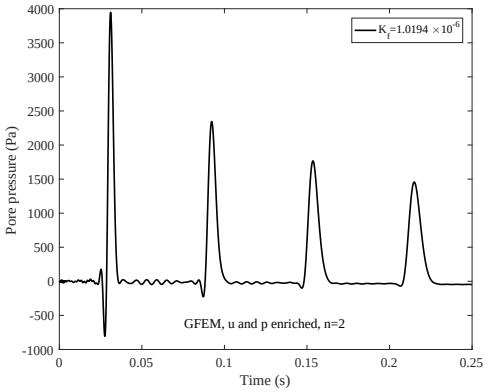


Figure 22: Time history of pore pressure under impact loading for $K_f = 1.0194 \times 10^{-6}$.

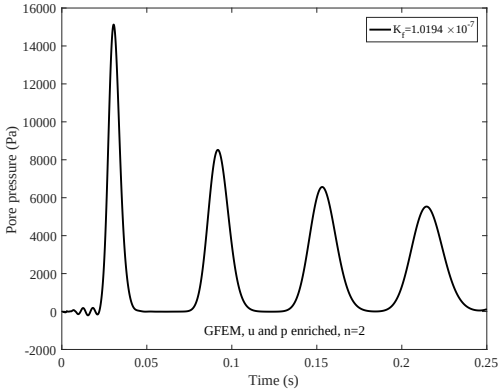


Figure 23: Time history of pore pressure under impact loading for $K_f = 1.0194 \times 10^{-7}$.

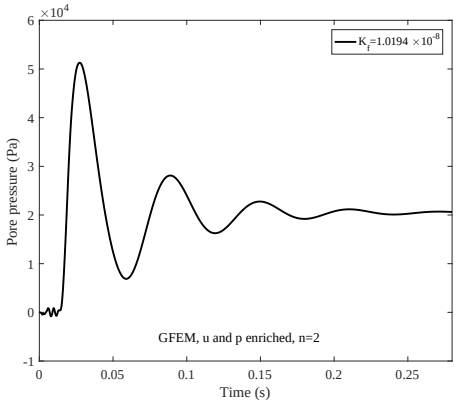


Figure 24: Time history of pore pressure under impact loading for $K_f = 1.0194 \times 10^{-8}$.

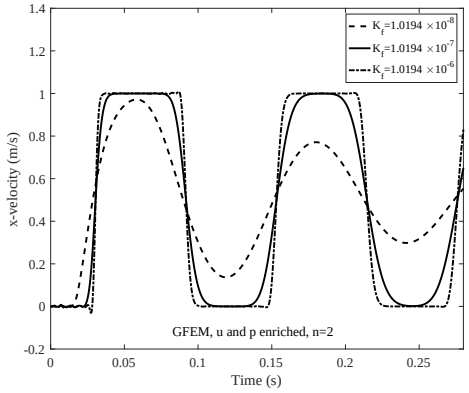


Figure 25: Time history of velocity under impact loading for various values of permeability.

reveals the crucial effect of diffusivity value on wave propagation behaviour. As is clear in the figures, decreasing the permeability of porous media results in the reduction of the frequency of pressure wave/pulse. Also, the long-term pore pressure is dependent on permeability. In other words, for low permeability media (Figure 24) there is a positive non-zero steady-state pore pressure. Whereas for the higher permeability cases (Figures 22 and 23) the pressure keeps its periodic trend of the wave pulse in which the peak value is monotonically decreasing. Moreover, the results show the highest rate of attenuation/dissipation for the lowest permeable case.

*5.6.2. Impact problem in fractured media*

To demonstrate the transient wave propagation response in a cracked porous media under impact loading (the same velocity impact loading of the earlier example is considered) and to investigate the interaction of hydro-mechanical wave pulse with fracture, a cracked poroelastic domain of $3m \times 0.5m$ with $k_f = 1.631 \times 10^{-6} m^3 s/kg$ is considered. Contact constraints across the fracture are satisfied through the ALM technique and the crack face are assumed to be impervious. The domain is discretized by a $20 \times 10$ rectangular mesh. A $0.3m$ long nearly vertical crack, inclinded at an angle of $3.6 \times 10^{-2}$ radians, is embedded in the media centered at $x = 1.1m$.

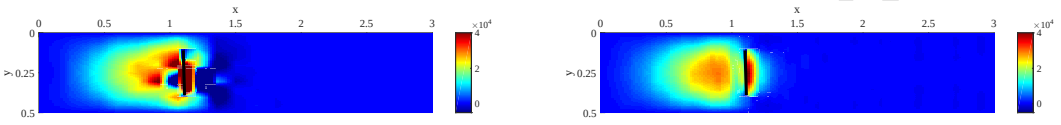

(a) using the conventional PNM (b) using the PNM-GFEM-M model with ($n = 1$)

Figure 26: Pore pressure signal in fractured porous media under impact loading at $t = 0.0092s$.

Figures 26a and 26b exhibit wave pattern for pore pressure distribution using the conventional PNM and the enriched PNM-GFEM-M model of this work ($n = 1$ for both displacement and pore pressure variables), respectively. As observed in these figures, in the case of the conventional PNM, the wave pattern (at a particular time) is noisy and asymmetric owing to numerical dispersions emerging from the regular polynomial interpolations used in conventional FEM. To be more clear, the interaction of the wave pulse and the impervious crack (when the wave front hits the crack surface) results in very abrupt and sharp spacial variation in the pore pressure distribution in the vicinity of the fracture. These sharp variations cannot be captured and modeled accurately using conventional interpolations, resulting in very severe numerical dispersion as seen in Figure 26a. Furthermore, the small amount of asymmetry introduced into the problem, by slightly inclining the fracture, leads to very asymmetric solution. Unlike the regular PNM, as seen in Figure 26b, using the developed PNM-GFEM-M leads to much more accurate and tangible results for the pore pressure contour of the interaction between the wave pulse and the crack. In addition, the PNM-GFEM-M solution is nearly symmetric, as would be expected for a nearly symmetric problem.

## 6. Conclusions

A two-variable ($u - p$) mixed Finite Element Model (FEM) has been developed for dynamic and wave propagation analysis of continuous and fractured porous media. General idea of the Phantom Node Method (PNM) is employed to introduce strong discontinuity of displacement and pore pressure across the crack faces. Trigonometric enrichments are included in the context of the Generalized Finite Element Method (GFEM) to rectify the problem of numerical dispersion that can appear in transient wave propagation simulation of porous media. This way, a new GFEM-enriched PNM mixed finite element model (i.e., PNM-GFEM-M) is developed for coupled dynamic hydro-mechanical simulation of saturated porous media. To satisfy the no-interpenetration condition along the crack faces and to simulate the frictional contact in stick/slip regimes, an Augmented Lagrange Multiplier Method is implemented.

Through various numerical examples, the effectiveness of the developed enriched FE model over conventional approaches is demonstrated. It has been demonstrated that the high-frequency numerical dispersions that may appear in regular FEM/PNM wave results (that are attributed to the Gibb's phenomenon) can be successfully suppressed in the hydro-mechanical wave propagation solutions of porous media using the enriched mixed FE model of this work. Moreover, it was shown that the most accurate wave results with the least amount of spurious oscillations are achieved when both the displacement and pore pressure fields are enriched with trigonometric interpolations; the larger the cutoff number for enrichments, the better the spurious oscillations are inhibited.

Lastly, some interesting hydro-mechanical features of the dynamic response of porous media are documented. When fluid is rapidly injected into a porous media, a non-monotonic response, characterized by a peak-pressure point in the injection pressure time history, is observed. This is in contrast to the monotonically-increasing trend of the injection pressure time history observed when fluid is injected slowly.

The developed Mixed GFEM-enriched Phantom Node Method (PNM-GFEM-M) is a promising model for the simulation of hydro-mechanical wave phenomena and transient dynamic behaviour in both continuous and fractured porous media. **It is worth mentioning that the proposed computational approach can be extended to moving cracks in applications like 3D hydraulic fracturing by**

**adding suitable crack propagation criterion and evolving the discontinuities by replacing the regular element with superimposed elements with additional phantom nodes at the locations where failure occurs and fracture advances.**

**The present article does not concentrate on the computational efficiency of the method for large-scale problems. Given the significant spurious oscillations which appear in the regular FE simulations (even with highly-refined meshes) of high-frequency waves or time-harmonic waves with small wavelengths and the notable capability of the presented enriched FE method to more accurately simulate the wave problems, a future investigation should address the cost-effectiveness of the enriched scheme for large-scale problems.**

**Acknowledgements**

The authors gratefully acknowledge the support of a Discovery Grant and a Strategic Grant from the Natural Sciences and Engineering Research Council of Canada (NSERC).

**References**


[1] Jha B, Juanes R, A locally conservative finite element framework for the simulation of coupled flow and reservoir geomechanics. *Acta Geotechnica*, 2(3), 139–153 (2007).

[2] Simon B, Wu J, Carlton M, Kazarian L, France E, Evans J, Zienkiewicz O, Poroelastic dynamic structural models of rhesus spinal motion segments. *Spine*, 10(6), 494–507 (1985).

[3] Levenston M, Frank E, Grodzinsky A, Variationally derived 3-field finite element formulations for quasistatic poroelastic analysis of hydrated biological tissues. *Computer Methods in Applied Mechanics and Engineering*, 156(1), 231246 (1998).

[4] Cowin SC, Bone poroelasticity. *Journal of Biomechanics*, 32(3), 217–238 (1999).

[5] Moeendarbary E, Valon L, Fritzsche M, Harris AR, Moulding DA, Thrasher AJ, Stride E, Mahadevan L, Charras GT, The cytoplasm of living cells behaves as a poroelastic material. *Nat Mater*, 12(3), 253261 (2013).

[6] Terzaghi K., Theoretical soil mechanics. *Wiley: New York*, (1943).

[7] Biot M.A., Mechanics of incremental deformations. *Wiley: Chichester*, (1965).

[8] Lotfian Z, Sivaselvan M.V., A topology-motivated mixed finite element method for dynamic response of porous media. *Int. J. Numer. Meth. Engng* , 00, 135 (2014).

[9] Dai N, Vafidis A, Kanasewich E. R., Wave propagation in heterogeneous porous media: A velocity-stress finite-difference method. *Geophysics* , 60(2), 327–340 (1995).

[10] Li C, Borja RI, Regueiro RA, Dynamics of porous media at finite strain. *Computer methods in applied mechanics and engineering* , 193(36), 3837–3870 (2004).

[11] Khoei, A.R., Extended finite element method: theory and applications. *John Wiley & Sons*, (2014).

[12] Zienkiewicz O, Shiomi T, Dynamic behavior of saturated porous media; the generalized Biot formulation and its numerical solution. *International journal for numerical and analytical methods in geomechanics*, 8(1), 71–96 (1984).

[13] Suh JK, Spilker R, Holmes M, A penalty finite element analysis for nonlinear mechanics of biphasic hydrated soft tissue under large deformation. *International Journal for Numerical Methods in Engineering*, 32(7), 1411– 1439 (1991).

[14] Zienkiewicz OC, Chan AHC, Pastor M, et al, Computational Geomechanics with Special Reference to Earthquake Engineering, *John Wiley & Sons, Inc, New York* (1999).

[15] Camacho-Tauta, J., Hassan, A., Cascante, G. and Viana da Fonseca, A., Experimental and Numerical Observations of the Frequency-Domain Method in Bender-Element Testing, *Journal of Geotechnical and Geoenvironmental Engineering*, 143:2:04016096 (2016).

[16] Remij E.W., Remmers J.J.C., Huyghe J.M., Smeulders D.M.J., The enhanced local pressure model for the accurate analysis of uid pressure driven fracture in porous materials, *Computer Methods in Applied Mechanics and Engineering*, 286, 293312 (2015).

[17] Nikolic M., Ibrahimbegovic A., Miscevic P., Discrete element model for the analysis of uid-saturated fractured poro-plastic medium based on sharp crack representation with embedded strong discontinuities, *Computer Methods in Applied Mechanics and Engineering*, 298, 407427 (2016).

[18] Rethore J., De Borst R., Abella M.A., A discrete model for the dynamic propagation of shear bands in a fluidsaturated medium. *International journal for numerical and analytical methods in geomechanics*, 31(2), 347–370 (2007).

[19] Armero F., Callari C., An analysis of strong discontinuities in a saturated poroplastic solid. *International journal for numerical methods in engineering*, 46(10), 1673–1698 (1999).

[20] Miehe C., Mauthe S., Phase feld modeling of fracture in multi-physics problems. Part III. Crack driving forces in hydro-poro-elasticity and hydraulic fracturing of uid-saturated porous media, *Computer Methods in Applied Mechanics and Engineering*, 304, 619655 (2016).

[21] Lee S., Mikelic A., Wheeler M. F., Wick T., Phase-field modeling of proppant-filled fractures in a poroelastic medium, *Computer Methods in Applied Mechanics and Engineering*, 312, 509541 (2016).

[22] Mobasher M.E., Berger-Vergiat L., Waisman H., Non-local formulation for transport and damage in porous media, *Computer Methods in Applied Mechanics and Engineering*, 324, 654688 (2017).

[23] Moës N., Dolbow J., Belytschko T., A finite element method for crack growth without remeshing. *International journal for numerical methods in engineering*, 46, 131–150 (1999).

[24] Melenk J.M., Babuška I., The partition of unity finite element method: Basic theory and applications. *Computer Methods in Applied Mechanics and Engineering*, 139, 289314 (1996).

[25] Vamaraju J., Sen M., De Basabe J. and Wheeler M., A comparison of continuous, discontinuous, and enriched Galerkin finite-element methods for elastic wave-propagation simulation. *SEG Technical Program Expanded Abstracts*, 4063–4067 (2017).

[26] Lee S., Wheeler M.F., Adaptive enriched Galerkin methods for miscible displacement problems with entropy residual stabilization. *Journal of Computational Physics*, 331, 19–37 (2017).

[27] Lee S., Lee Y.J., Wheeler M.F., A locally conservative enriched Galerkin approximation and efficient solver for elliptic and parabolic problems. *SIAM Journal on Scientific Computing*, 38(3), A1404–A1429 (2016).

[28] Jeong-Hoon Song, Pedro M. A. Areias, Belytschko T. A method for dynamic crack and shear band propagation with phantom nodes. *International Journal for Numerical Methods in Engineering*, 67, 868893 (2006).

[29] Anita Hansbo, Peter Hansbo. A finite element method for the simulation of strong and weak discontinuities in solid mechanics. *Computer Methods in Applied Mechanics and Engineering* , 193, 35233540 (2004).

[30] Ji H., Dolbow J. E., On strategies for enforcing interfacial constraints and evaluating jump conditions with the extended finite element method. *International Journal for Numerical Methods in Engineering*, 61(14), 2508–2535 (2004).

[31] Moës N., Béchet E., Tourbier M., Imposing Dirichlet boundary conditions in the extended finite element method. *International Journal for Numerical Methods in Engineering*, 67(12), 1641–1669 (2006).

[32] Hautefeuille M., Annavarapu C., Dolbow J.E., Robust imposition of Dirichlet boundary conditions on embedded surfaces. *International Journal for Numerical Methods in Engineering*, 90(1), 40–64 (2012).

[33] Hirmand M., Vahab M., Khoei A. R., An augmented Lagrangian contact formulation for frictional discontinuities with the extended finite element method, *Finite Elements in Analysis and Design*, 107, 28–43 (2015).

[34] Kohno H., Bathe K. J., Wright J. C., A finite element procedure for multiscale wave equations with application to plasma waves. *Computers & Structures*, 88, 8794 (2010).

[35] Ham S., Bathe K. J., A finite element method enriched for wave propagation problems, *Computers & Structures*, 94-95, 1–12 (2012).

[36] Komijani M, Gracie R., An enriched finite element model for wave propagation in fractured media, *Finite Elements in Analysis and Design*, 125, 14–23 (2017).